Bachelorthesis

# Electron-positron pair production from the Cosmic Photon Background

Sean Penny

Würzburg, January 21, 2025

Julius-Maximilians-Universität Würzburg
Lehrstuhl für Astronomie
Betreuer: Dr. Thomas Siegert

# Abstract

Throughout the Universe, many different astronomical objects and mechanisms produce high-energy photons flying around in all directions. An electron-positron pair can be created by two of these photons colliding and meeting the electron-positron threshold, a rule which holds true everywhere. In this thesis the Cosmic Photon Background (CPB) is studied from the radio frequency to the high-energy $\gamma$-frequency of photons to estimate the isotropic pair-production rate and subsequent annihilation of electron-positron pairs. The resulting decomposition of the CPB into black bodies in combination with the analytical integral by Böttcher & Schlickeiser (1997) is used to calculate the $\gamma$-$\gamma$ pair production rate resulting from the interaction of the CPBs photons with eachother for a wide energy spectrum of positrons. In the case of the CPB interacting with itself, the pair production process results in a total injection over the energy spectrum of $Q = (2.0 \pm 0.5) \cdot 10^{-36}\,\frac{\mathrm{e}^+}{\mathrm{cm}^3\mathrm{s}}$. Further, the pair production produced by the emission of other bodies, such as the Sun, the planets of the solar system and the Milky Way, is calculated and studied as observed from Earth. An estimate about the positron production of the Milky Way‘s radiation is made in the range of infrared to ultraviolet, to see whether it outshines the positron production yielded by the CPB radiation. From the resulting energy spectrum of the produced positrons $e^+$, their energy loss and diffusion in the Intergalactic Medium (IGM) is examined and from this their diffusion time scale $T_{\mathrm{diff}}$ and diffusion length scale $\lambda_{\mathrm{D}}$ necessary for the thermalization are calculated. Lastly, the time scale for the annihilation of thermalized positrons with free electrons in the IGM is determined, to evaluate the total time from injection of the positrons to their annihilation for different positron energies. This leaves $3.3 \cdot 10^{-4}$ of created positrons within a timescale of 1 Gyr viable for annihilation, from which the annihilation flux is calculated. The CPB reacting with itself contributes an isotropic 511 keV line flux of $F_{511} = (1.0 \pm 0.1) \cdot 10^{-10}\,\frac{\mathrm{ph}}{\mathrm{s\,cm}^2}$. Compared to the flux of a Galactic bulge-only model of $F = (0.96 \pm 0.06) \cdot 10^{-3}\,\frac{\mathrm{ph}}{\mathrm{s\,cm}^2}$ (Weidenspointner et al., 2007), the CPB's contribution would be hard to detect even with highly precise next-generation $\gamma$-ray telescopes. Furthermore, the $\gamma$-ray component of the CPB also outshines $F_{511}$ by magnitudes.

**Key words:** Cosmic Photon Background - Blackbody radiation - Photon-photon interaction - Pair-production - Diffusion-loss equation

# Contents

# Chapter 1

# Introduction

After the first discovery of the 511 keV $\gamma$-rays from our Galactic centre via a high-altitude balloon altitude observation in 1970 (Johnson et al., 1972), the study of this emission and its source has gained significant attention. Although the Johnson observation could not exactly pinpoint the energy of the emission as 511 keV, it only took a few extra years to determine the narrow line to be at 511 keV with a FWHM of 3.2 keV, as the emission of the electron-positron annihilation (Leventhal et al., 1978). If the source of the emission is fuelled by positrons, then the question becomes: Where do the necessary particles come from?

Three decades after the Leventhal observation, the flux of 511 keV could be measured at $\sim 10^{-3}\,\frac{\mathrm{ph}}{\mathrm{cm}^2\mathrm{s}}$ in the Galactic bulge by the SPI spectrometer from the INTErnational Gamma-Ray Astrophysics Laboratory SPI/INTEGRAL. This results in $\sim 10^{43}$ positrons per second annihilated in this region (Weidenspointner et al., 2008).

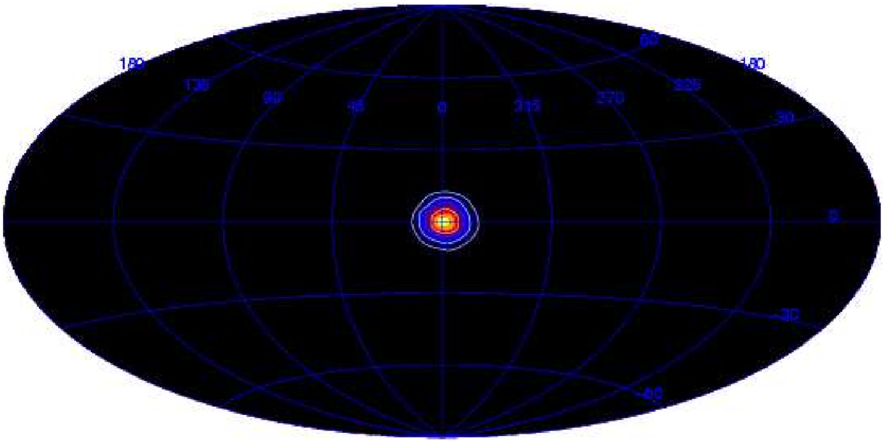

**Figure 1.1:** Depicted is a sky map of the 511 keV line from electron-positron annihilation from Weidenspointner et al. (2007). The centroid of emissions is close to the Galactic centre.

Figure 1.1 shows a sky map of the 511 keV electron positron annihilation line, in which the bulk of the emission comes from close to the centre of the Milky Way Galactic centre. The total flux in this specific map is $1.0 \cdot 10^{-3}\,\frac{\mathrm{ph}}{\mathrm{cm^2 s}}$ (Weidenspointner et al., 2007). There are now many observations and hypotheses for possible sources of the positrons within our Galaxy, for example low mass X-ray binaries (LXMBs). The distribution of general LXMBs peaks in the bulge region, while LXMBs specifically also have an imbalance in their disk distribution, corresponding to the asymmetry in the 511 keV emission from the Galactic disk (Weidenspointner et al., 2008), although it has to be noted, that the asymmetry may be a product of exposure effects.

As positrons play a key role in various different astrophysical phenomena, like dark matter searches, cosmic ray interactions and the behaviour of high-energy processes in the vicinity of compact objects such as neutron stars and black holes, it is crucial to understand possible background processes creating positrons, which could interfere with the above mentioned types of research. One such background process would be the pair production by high-energy photon-photon collisions with photons being emitted by the CPB. This production mechanism not only gives insight into the CPB itself, but also might reveal critical information about positron production on a larger scale. By better understanding background sources, future observation technologies and methods could be optimized around this knowledge.

The main focus of this thesis will be the background production throughout the local Universe via the CPB interacting with itself. However, interactions of the CPB with other photon fields as emitted by the Sun, our surrounding planets and the Milky Way will be estimated. To study the impact, that the annihilation of these produced positrons would have on other research, the diffusion and loss of energy of the positrons throughout the Intergalactic Medium (IGM) will be studied, to derive the flux of 511 keV photons produced by this particular background process.

This thesis is structured as follows: Chapter 2 goes over the theoretical knowledge needed, with 2.1 being an overview of the composition of the CPB, 2.2 being an explanation of the idea of pair-production, where the concept stems from and how it is utilised in this thesis and 2.3 is a derivation of the diffusion-loss equation and energy-loss terms for positrons moving through the IGM, as necessary for this thesis.

Chapter 3 explains the blackbody, how it is used to describe the Cosmic Microwave Background (CMB) and how it can be used to decompose the entire CPB (3.1). 3.2 explains the way a sum of black bodies is fitted to the CPB spectrum.

Chapter 4 derives the pair-production integral and explains how it is calculated and how resulting errors are treated.

Chapter 5 presents the results calculated with the aforementioned integral in three sections. 5.1 goes through the pair-production yield from the CPB interacting with itself. 5.2 estimates the fluxes of positrons produced by the bodies of the Solar System interacting

with CPB as seen from earth and compares with the results from 5.1. 5.3 compares the estimated Milky Way positron production through CPB interaction with the results from 5.1.
Chapter 6 analyses how positrons produced in 5.1 propagate through the IGM, while losing energy. By analysing the way these positrons annihilate in the IGM, their flux of 511 keV photons can be derived.

# Chapter 2

# Theoretical prerequisites

So the main two theoretical components, that follow from the above considerations are the CPB and the $\gamma$-$\gamma$ pair-production. The pair-production process is what ultimately results in the positrons, that are of interest for the creation of 511 keV photons via the inverse process of annihilation and the CPB is the Universe-wide emitter of the photons, which are needed for this process to occur. Beyond this, the diffusion-loss equation is also discussed to better understand how relevant these "background-positrons" are for the phenomenon of the 511 keV line. It is relevant to deduce the positrons diffusion time and length scales within the IGM. By additionally looking at the annihilation time from the moment of thermalization, the applicable energy range of positrons, that annihilate in a reasonable time frame ($\sim$ 1 Gyr), within a reasonable distance of a few 100 Mpc, as to avoid cosmological considerations, can be determined. As will become apparent (chapter 6) later, the diffusion and annihilation time of high energy positrons can become quite large, depending on the parameters of the IGM, which results in only a fraction of the injected positrons being viable for 511 keV photon production without the consideration of cosmological redshift. Lastly, a quick overview of the IGM and the way it is approximated and used is given.

## 2.1 The Cosmic Photon Background (CPB)

The CPB describes the entire spectrum of electromagnetic diffuse isotropic background radiation spanning throughout the Universe, as observed from the Earth today. These background photons occupy a very large spectrum with frequencies $\nu$ ranging from orders of magnitude around $10^8$ Hz to $10^{25}$ Hz. Further, the CPB is homogeneous and isotropic throughout the universe (Hill et al, 2018).

The study of the CPB properly started when the microwave component (CMB) of the CPB was discovered in 1965 (Penzias & Wilson, 1965; Dicke et al, 1965), which is now the

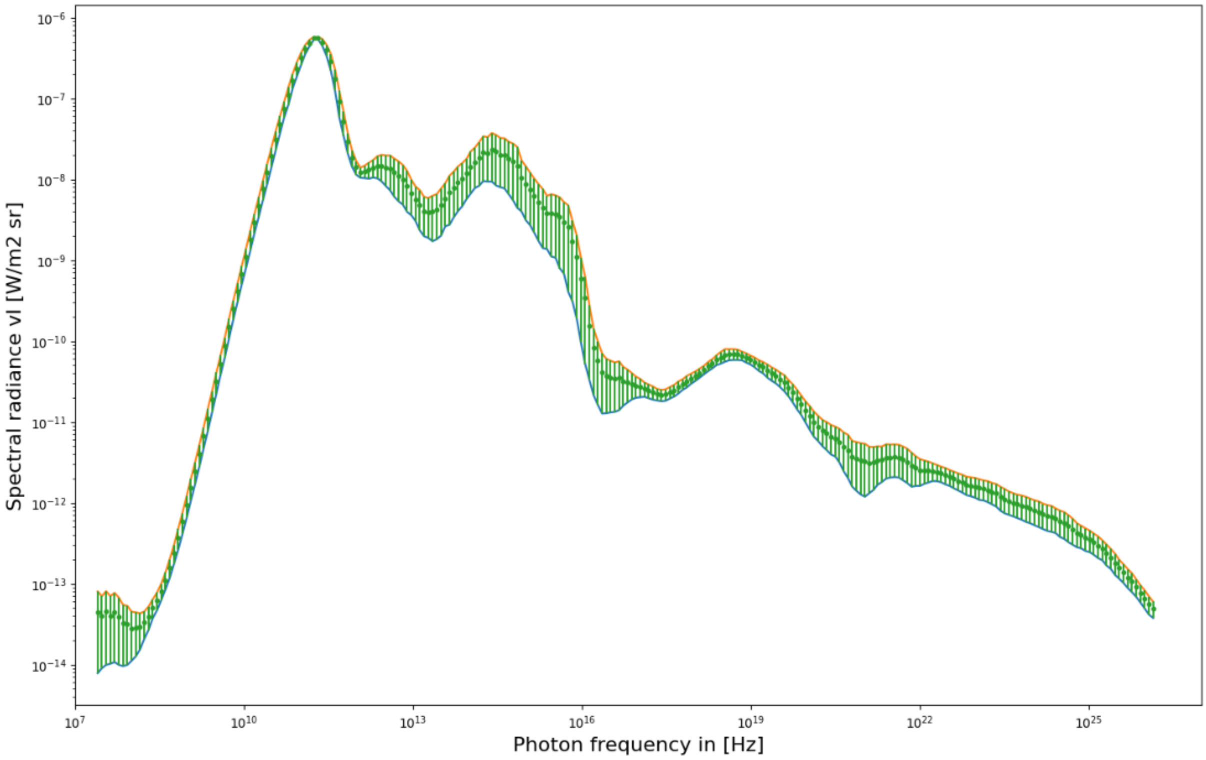

**Figure 2.1:** Spectrum of the CPB showing the spectral radiance $\nu I_\nu$ in relation to the photon frequencies on a double-log scale (Hill et al, 2018). The range of spectral radiance is as measured can be seen. For example the CMB component ($10^{11}$ Hz) has almost no uncertainty, while components like the COB to CUB ($10^{14}$-$10^{16}$ Hz) show large uncertainties. This spectrum is used for the fit of the photon number density.

best understood and observed component. The CMB is the left over blackbody radiation from the Universe's early, hot phase, which has now cooled down to 2.7255 K (Hill et al, 2018). The fact, that the CMB can be modelled by an ideal blackbody will come back into consideration in section 3.1, when trying to find a model for the entire spectrum of the CPB. The spectrum can be roughly divided into the components listed in Table 1.

The sources of the different components and our current understanding of the same vary by up to 1-2 orders of magnitude. The methods by which these components are measured also have substantial differences, resulting in parts, that have very precise data (e.g. CMB, CXB) and other parts, that require models and extrapolations to estimate their contribution (e.g. CRB, COB), as can be seen in Figure 2.1.

Starting at the CRB, the standing idea is, that the sources for this component consist of mainly synchrotron emissions by the magnetic fields of galaxies and AGN emissions. When measuring the CRB, the plasma frequencies of the Earth, Milky Way and Interstellar medium (ISM) become hindrances as they reflect the radio-photons at about 10 MHz for the earths atmosphere and at around 1 MHz for the ISM (Lagache et al, 2005), basically

| Name | Frequencies (Hz) |
|---|---|
| Radiowaves (CRB) | $< 10^{10}$ |
| Microwaves (CMB) | $10^{10}$-$10^{12}$ |
| Infrared (CIB) | $10^{12}$-$10^{14}$ |
| Optical (COB) | $10^{14}$-$10^{15}$ |
| Ultraviolet (CUB) | $10^{15}$-$10^{16}$ |
| X-rays (CXB) | $10^{16}$-$10^{19}$ |
| $\gamma$-rays (CGB) | $> 10^{19}$ |

**Table 2.1:** The table shows a rough divide of the components of the CPB and their section of the frequency spectrum (Hill et al, 2018).

causing the spectrum to have a low-frequency observation limit.

The emissions in the infrared (CIB) mainly stem from heated dust in and around galaxies (Lagache et al, 2005). One can easily see, how directly measuring the CIB becomes heavily obscured by dust and planets close to our own solar system and even the dust present in the Milky Way, resulting in a less precise measurement. Lower bounds, for example, can be gained by only measuring the flux of resolvable galaxies, including extrapolations for fainter and therefore undetected sources, which is all summed. For upper bounds of the CIB on the other hand, the spectra of $\gamma$-ray emitting objects, like for example blazars are taken into account. These should have missing photons, which can interact with CIB photons, creating an electron-positron pair in the process, as will be discussed in the next section (Hill et al, 2018).

Since observations of the sky began with human eyes, the optical emissions of the Universe have been important for the longest time. Most of the radiance of the COB component comes from stars, which is the reason why its study is relevant for our understanding of star formation throughout the history of the Universe. As the emission from galactic dust also reaches into the optical range of the spectrum, they make measurements of the COB more challenging. Bounds in this case are given mainly by counting and summing over various datasets of optical light sources like stars and galaxies (Hill et al, 2018). The COB, and next also the CUB, are relatively important components for this thesis, as they both make up the main source of positron production by the CPB via interaction with the CGB component (section 5.1).

The CUB is the most difficult component to measure, as the hydrogen of the ISM is highly efficient in absorbing these wavelengths around $10^{15} - 10^{16}$ Hz. Furthermore, any measurement tools must also leave Earth‘s atmosphere to work properly. Estimates of this components upper bounds stem from flux measurement between 1970 to 1990, as they not only counted the background flux but also all other sources like the galaxy contributions. By counting UV sources, lower limits have been estimated. The origin of this frequency range consists of mostly young, hot stars and interstellar nebulae scattering emissions (Hill et al, 2018).

The CXB spans across a wider frequency range from $10^{16}$ Hz to $10^{19}$ Hz, than any of the previous components, which is the reason why different sources are assigned to the higher and lower end of the spectrum. For the lower end of the CXB, the main contributor is leftover thermal energy from the early Universe and heated dust in addition to nuclear energy from the fusion processes in the cores of stars (Hill et al, 2018). Moving into the higher energy end of the CXB towards the $\gamma$-range, processes in the accretion disks of AGNs (Active Galactic Nucleus) dominate the emission. This accretion of gas can become hot enough to emit thermal Bremsstrahlung photons in the higher X-ray range (Hill et al, 2018).

The transition between CXB and CGB around the 511 keV photon energy, is of great importance, as it offers a direct comparison for the results of this thesis in chapter 6, where a flux of 511 keV photons and the annihilation spectrum are calculated.

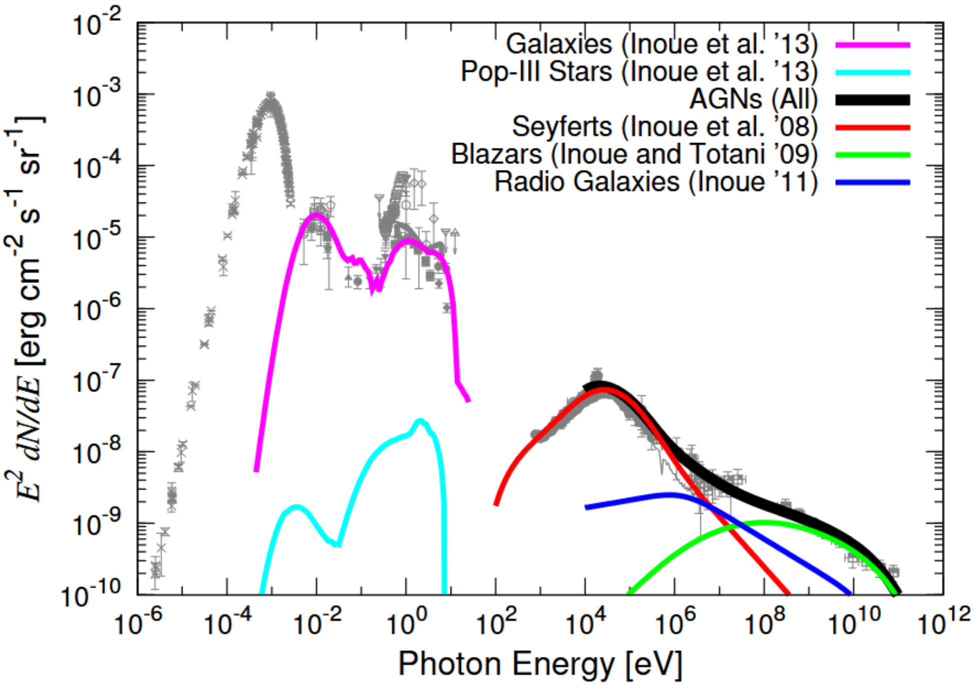

**Figure 2.2:** Contribution to the CPB by various sources (Inoue, 2014). Mainly of interest here are the Seyfert Galaxies, Blazars and Radio Galaxies, in the CXB to CGB range.

Looking at Figure 2.2, large contributions to the CXB and CGB are made by AGNs, with Seyfert Galaxies in the CXB range and with Radio Galaxies and Blazars in the CGB range. Seyfert Galaxies are spiral Galaxies with exceptionally nuclei, although

lower-luminosity, than other types of AGN. There distinguishing feature from quasars is having a quasar-like core, but with a clearly detectable host galaxy. They come in two types: Seyfert 1, with both broad and narrow lines in their spectrum, while Seyfert 2 are missing the broad lines (Petrov, 2004). In comparison, Radio Galaxies are mostly elliptical galaxies creating strong radio synchrotron emissions. Radio Galaxies can be categorised in broad-line (BLRG) and narrow-line (NLRG) types similarly to the Seyferts (Petrov, 2004). Finally blazars are AGNs mainly categorised by their strong emission variability and optical polarization. Blazars move towards earth with relativistic speeds, boosting one of their jets in observations from Earth (Petrov, 2004). Typical spectra of different types of AGNs can be seen at the end of this section in Figure 2.4.
At photon energies of $5 \cdot 10^5$ eV, the largest contribution in this lineup are the Seyferts, which can be seen in detail in Figure 2.3.

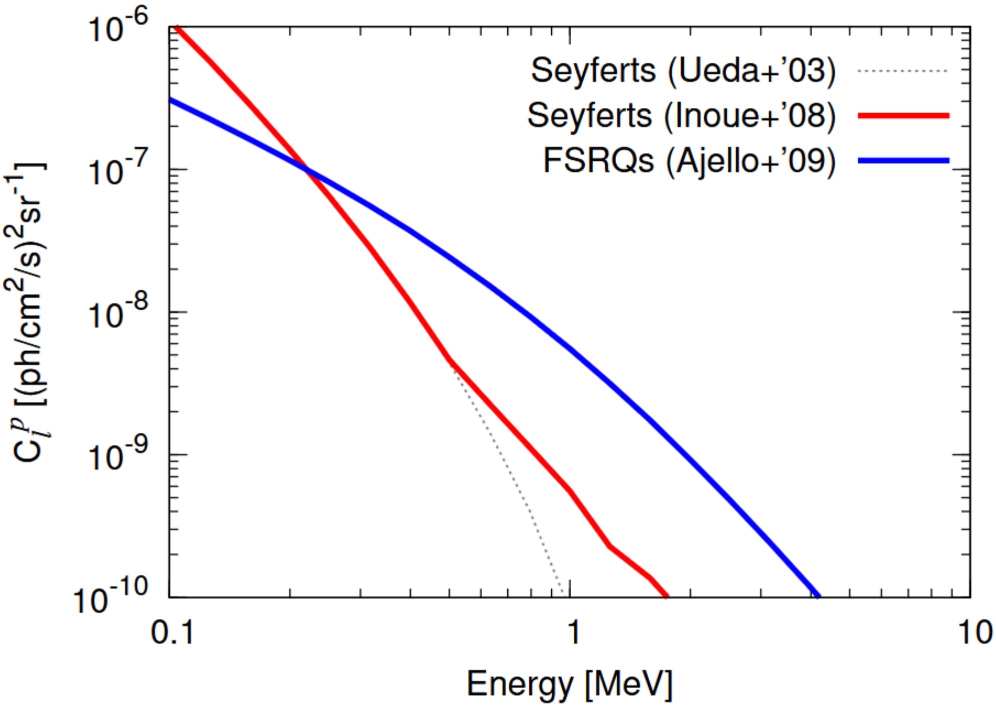

**Figure 2.3:** The above shows expected Poisson terms of the angular power spectrum of Seyferts and FSRQ‘s (Flat Spectrum Radio Quasars) at 200 keV-10 MeV (Inoue, 2014).

The CGB encompasses the largest frequency spectrum of all the components (everything above $10^{19}$ Hz), with a cutoff occurring towards the end of the spectrum, as most high energy $\gamma$-ray photons have been converted to particles by interacting with CIB photons along the long travel distance to Earth. As explained previously, the source of the CGB is made up of blazars and quasars. These high-energy particles can collide with photons in Compton scattering, supplying them with large amounts of energy. A small contribution also comes from supernovae explosions. Their large release of energy also contains $\gamma$-ray

photons (Hill et al, 2018).
Understanding the CPB is not only relevant for the work of this thesis, but is of further importance in the search for yet unknown phenomena, such as dark matter.

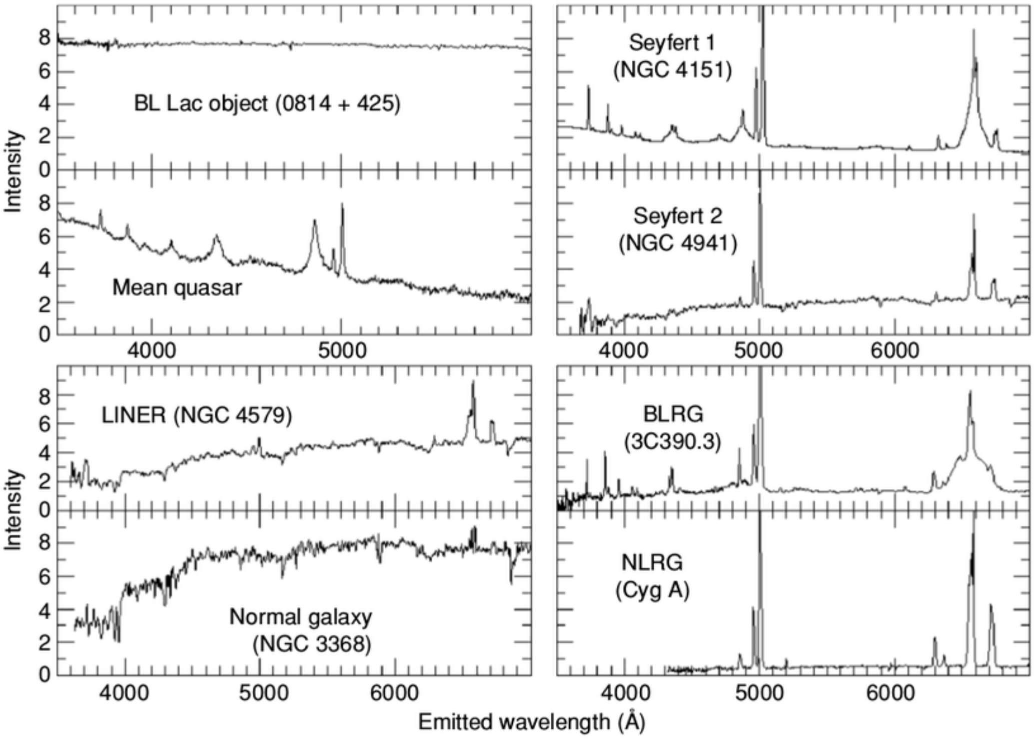

**Figure 2.4:** A depiction of typical spectra of different AGN types (Andika, 2016).

## 2.2 The pair production process

A milestone in quantum mechanics had been set with the postulation of Schrödinger‘s equation. It itself is asymmetric with respect to time and space and has no links to special relativity yet. Many attempts had been made to bring Schrödinger‘s equation into accordance with special relativity, for example the Klein-Gordon equation, proposed in part by Schrödinger himself. This solution predicted, that the total probability of a particles position anywhere within the Universe changed with time, which was then thought to be unacceptable (Atkins, 1991).
Dirac attempted a solution by forcing the space derivative to be of first-order, although conditions had to be set, to keep the equation in accordance with the successful Schrödinger equation for non-relativistic speeds. These conditions lead to wavefunctions of four components, two of which hold the positive energy of a particle at rest, while the other two ended up implying a negative energy for a particle. As these unfitting solutions are still mathematically viable, Dirac had to find a fitting interpretation. He therefore proposed, that the entirety of negative energy eigenstates throughout the Universe are

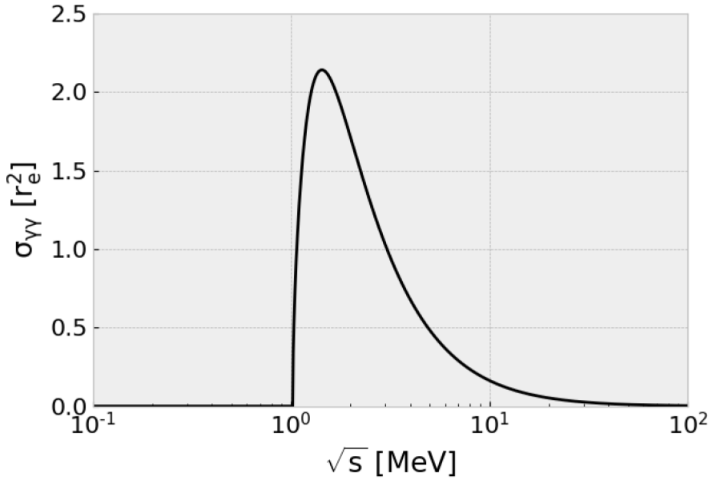

**Figure 2.5:** The figure portrays the cross section for the linear Breit-Wheeler process depending on $\sqrt{\mathrm{s}} = 2\epsilon_1\epsilon_2(1 - \cos\theta_\mu)$ (as seen in chapter 4) in units of the classical electron radius $\mathrm{r_e} = 2.8 \cdot 10^{-13}\,\mathrm{cm}$ (Esnault et al., 2021).

filled, so only the positive energy particles could be experienced. This meant, that if a particle in a negative energy eigenstate is excited out of said eigenstate, it leaves a “hole” with positive charge and a net positive mass. At the time Dirac interpreted this particle to be the proton (Atkins, 1991).

This can be seen in Dirac (1930), where the misunderstanding still stands and some mass-terms stay vague, as to if they are the electrons mass, the protons mass or a mean of both. But the paper lays the groundwork for the idea of the now-relevant electron-positron annihilation into a pair of $\gamma$-photons. In Dirac (1931) the negative energy “holes” are reinterpreted as a new kind of particle - the anti-electron - in light of the investigation, that this particle would need the mass of an electron rather than that of a proton. Further, he postulated the idea most relevant for this thesis: The inverse of the annihilation process, where two high-energy $\gamma$-ray photons collide, producing an electron and a positron at the same time (Dirac, 1931).

G. Breit and John A. Wheeler continued on this idea of matter creation through light quanta interaction (Breit & Wheeler, 1934) by calculating the probability of the process.

$$\gamma + \gamma' \rightarrow \mathrm{e}^- + \mathrm{e}^+ \tag{2.1}$$

The simplest version, involving only two photons (Figure 2.6), had been considered to be of little interest for observation in experiments on Earth, as the cross section is very small ($\sim 10^{-26}\,\mathrm{cm}^2$ as seen in Figure 2.5) and the technical feasibility of the necessary high-energy and high-density lasers is rather poor (Breit & Wheeler, 1934). Photons need energies at least in the MeV realm and the energy densities of lasers for sufficient pair yield ($\sim 10^7$ pairs) are in the order of magnitude of $10^{22} - 10^{23}\,\frac{\mathrm{W}}{\mathrm{cm}^2}$ (He et al., 2022). This is in part because of the equivalence of mass and energy, making it necessary for the photons to have a combined energy of at least the produced mass $E = 2m_ec^2 \approx 1.022\,\mathrm{MeV}$.

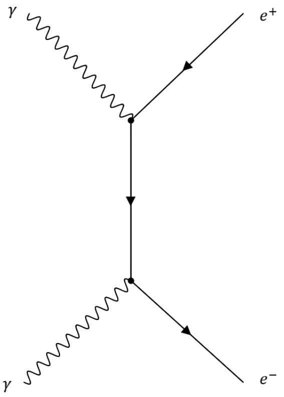

**Figure 2.6:** Simplest Feynman diagram describing the collision of two photons, creating and electron-positron pair, the so called linear Breit-Wheeler process.

There is also the nonlinear Breit-Wheeler process, in which a singular high-energy probe photon decays into the electron-positron pair within the presence of a strong electromagnetic field in form of laser pulses for example (Titov et al., 2013). Although this process is easier to observe in a laboratory and this has been done, it is not going to be considered further for this thesis. The conditions, that cannot realistically be met on Earth are, however, more realistic to be present in outer space, where the CPB supplies the high-energy photons for example. The cross section of the linear Breit-Wheeler process can be found in section 4 (4.2), where it is implemented.

## 2.3 The diffusion-loss equation

Once the positrons have been created, they are charged particles moving through space with a certain energy spectrum, governed by the injection rate of the process. Therefore they become subject to different interactions within the IGM through which they lose energy, such as by Inverse Compton scattering, synchrotron radiation, Bremsstrahlung and Coulomb interactions (Prantzos et al., 2010). The particles can then be considered to diffuse throughout the medium, described by a diffusion coefficient $D_0$. The energy spectrum of these particles can be described at different points in the IGM with the differential diffusion-loss equation. In a volume $dV$, where particles are injected at the rate $Q(E,t)dV$, their energy gains and losses are described by

$$-\frac{dE}{dt} = b(E). \tag{2.2}$$

E is the energy of the positrons and $b(E)$ includes all the interactions mentioned above, through which the positrons lose energy. Looking at the spectrum of particles $N(E)dE$ at the time $t$ without any injection rate for now, there are $N(E)\Delta E$ particles in the range $E+\Delta E$. Moving in time to $t+\Delta t$ the particles are substituted by those, that had energies within $E' + \Delta E'$ at the time $t$

$$E' = E + b(E)\Delta t, \tag{2.3}$$

$$E' + \Delta E' = (E + \Delta E) + b(E + \Delta E)\Delta t. \tag{2.4}$$

For small $\Delta E$ values these equations can be subtracted to

$$\Delta E' = \Delta E + \frac{db(E)}{dE}\Delta E \Delta t. \tag{2.5}$$

With the change in energy with $\Delta t$ the change in particle number becomes

$$\Delta N(E)\Delta E = -N(E,t)\Delta E + N[E + b(E)\Delta t, t]\Delta E'. \tag{2.6}$$

For small $b(E)\Delta t$ values and substituting for $\Delta E'$, we get the change of the positron spectrum in the volume $dV$ caused by $b(E)$ as

$$\frac{dN(E)}{dt} = \frac{d}{dE}[b(E)N(E)]. \tag{2.7}$$

Now the injection rate can be reintroduced by

$$\frac{dN(E)}{dt} = \frac{d}{dE}[b(E)N(E)] + Q(E,t). \tag{2.8}$$

Usually this equation also contains the change of particles in $dV$ by diffusion with the extra term $+D_0\nabla^2 N(E)$, but as the density of produced positrons by the CPB does not change with location throughout the Universe, the diffusion term becomes zero (Longair, 2011).

$Q(E,t)$ will later be described by the results of the pair-production yield integral, therefore what is left to determine is the energy loss function $b(E) = -\frac{dE}{dt}$.

Starting in the lower energy range of positrons ($< 1\,\mathrm{GeV}$), they mainly lose their energy through collisions with free electrons of the IGM in this case. An approximation for the energy loss (in $\frac{eV}{s}$) in the cold plasma case mainly depending on the electron density $n_e$ is given by:

$$\left(\frac{dE}{dt}\right)_{Cou} = -7.7 \cdot 10^{-9}\,\frac{n_e}{\beta}\left[\ln\left(\frac{\gamma}{n_e}\right) + 73.6\right] \tag{2.9}$$

with $\gamma$ here and in the following being the Lorentz factor of the positrons and $\beta = \frac{v(E)}{c}$ therefore being given by $\beta = \sqrt{1 - \frac{1}{\gamma^2}}$ (Prantzos et al., 2010). For the electron density value $n_e$, values from $10^{-6}\,\frac{e^-}{cm^3}$ to $10^{-4}\,\frac{e^-}{cm^3}$ will be used, to approximate the IGM.

Positrons moving through the IGM with higher energies (1-10 GeV) also lose energy by interacting with electrons, ions and atoms by emitting bremsstrahlung. For the following calculations, we approximate the IGM as a purely ionized hydrogen gas for which we get the following energy loss:

$$\left(\frac{dE}{dt}\right)_{BR} = -3.6 \cdot 10^{-11} Z(Z+1)\gamma\, n_{IGM} \left[\ln(2\gamma) - \frac{1}{3}\right] \tag{2.10}$$

Here Z is the charge number of the ions, so Z=1 for hydrogen, and $n_{IGM}$ is the ion density in the IGM (Prantzos et al., 2010).
For an existing magnetic field B in the IGM, ultrarelativistic positrons ($> 10\,\mathrm{GeV}$) also emit synchrotron radiation, thus losing energy. The energy loss is described by:

$$\left(\frac{dE}{dt}\right)_{Syn} = -9.9 \cdot 10^{-16}\, B^2\gamma^2\beta^2 \cdot \frac{2}{3} \tag{2.11}$$

B for this equation is given in $\mu G$ and the factor $\frac{2}{3}$ is the average over the pitch angle distribution in Prantzos et al. (2010).
The second mechanism for ultrarelativistic positrons losing energy is the Inverse Compton scattering from background photons. As already shown in section 2.1, the most dominant component in terms of density of photons is the CMB. For the Inverse Compton scattering with CMB photons with $\mathrm{h}\nu << \mathrm{m_e c^2}$ the energy loss is given by:

$$\left(\frac{dE}{dt}\right)_{IC} = -2.6 \cdot 10^{-14}\, u_{rad}\gamma^2\beta^2 \tag{2.12}$$

with $u_{rad}$ being the radiation energy density of the CMB ($= 0.26\,\frac{eV}{cm^3}$) (Prantzos et al., 2010). Certainly, one may include other components of the CPB in this energy density or even the radiation of the Milky Way, but as will be discussed at the end of this chapter, other parameters of the IGM are also going to be set, to estimate the lower bound of energy loss in the IGM, therefore $u_{\mathrm{rad}}$ is chosen as a lower bound of energy density as well.
The entire energy loss is then given by $b(E) = -\sum_i \left(\frac{dE}{dt}\right)_i$, which can be written as follows:

$$\begin{aligned} b(E) =& 7.7 \cdot 10^{-9} \frac{n_e\gamma}{\sqrt{\gamma^2-1}} \left(ln\left(\frac{\gamma}{n_e}\right) + 73.6\right) \cdot \gamma\sqrt{\gamma^2-1}\cdot \\ & \cdot (6.6 \cdot 10^{-16}\, B^2 + 2.6 \cdot 10^{-14} u_{rad}) \cdot 3.6 \cdot 10^{-11}\, n_{\mathrm{IGM}}\, \gamma \left(ln(2\gamma) - \frac{1}{3}\right) \end{aligned} \tag{2.13}$$

An example for the b(E) with a set of parameters is shown in Figure 2.7.

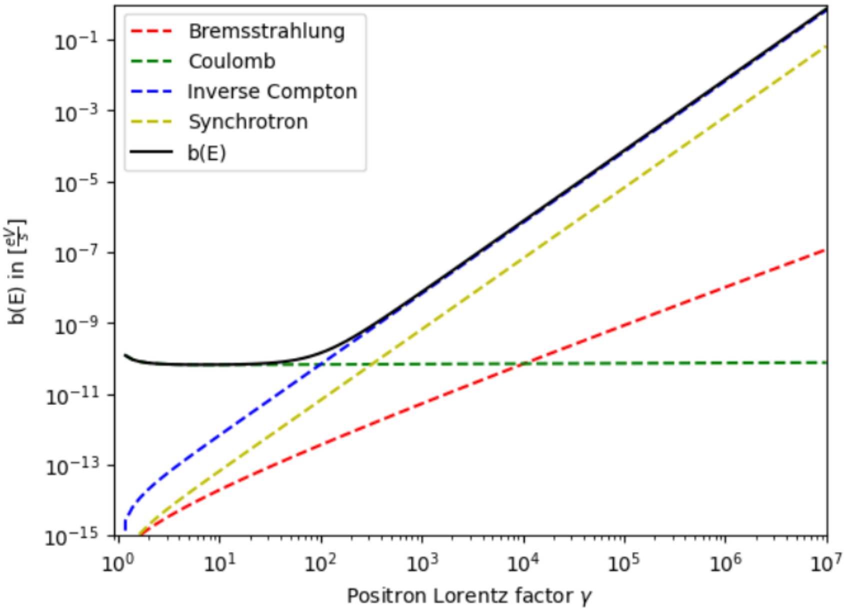

**Figure 2.7:** Above, b(E) is shown with the components that make up the energy loss function. As parameters the following is used: $n_e = 10^{-4}\,\frac{e^-}{cm^3}$, B=1 $\mu G$ and $n_{\rm IGM} = 10^{-5}\,\frac{1}{cm^3}$.

To summarize the assumptions and approximations made about and used for the IGM. This will become relevant in Chapter 6, when calculating the time necessary for produced positrons to thermalize in the IGM $T_{\rm loss}$ and the time they need to annihilate once thermalized $\tau_{\rm ann}$.
The matter is assumed to be fully ionized hydrogen with a density of $n_{IGM} = 10^{-5}\,\frac{1}{cm^3}$. As the electrons density directly correlates to the impact of Coulomb interactions on the energy loss of positrons (Figure 2.7 green), an array of values is used with $10^{-6}\,\frac{e^-}{cm^3}$, $10^{-5}\,\frac{e^-}{cm^3}$ and $10^{-4}\,\frac{e^-}{cm^3}$. The photons for Inverse Compton scattering in b(E) are solely contributed by the CMB in this approximation, resulting in an energy density of $u_{rad} = 0.26\,\frac{eV}{cm^3}$. Lastly, the magnetic field responsible for the energy loss through synchrotron radiation is set to B=1 $\mu G$. Furthermore the temperature of the IGM determines the thermalization energy $E_{th}$ of the positrons and therefore the diffusion time scale $T_{loss}$ and annihilation time scale $\tau_{ann}$. In light of this, temperatures from $10^4$ K to $10^7$ K are tested.

# Chapter 3

# Photon density distribution of the Cosmic Photon Background

The main attribute of the CPB, that will be needed to calculate the pair-production yield from the CPB's interaction with itself or even with other sources, is the photon density $n_{ph}(\epsilon_i)$ with photon energies $\epsilon_i$, where i numbers the two photons of the interaction. Therefore this section will explain, how the entire CPB is modelled and how a set of parameters is fitted. The data used for the fit is shown in Figure 2.1 from (Hill et al, 2018).

## 3.1 Decomposition of CPB into black bodies

As mentioned before, a blackbody emitter perfectly describes the CMB component of the CPB, as can be seen in Figure 3.1. A blackbody‘s spectral radiance $\mathrm{I}_\nu$ is described by

$$I_\nu(\nu, T) = \frac{2h\nu^3}{c^2} \frac{1}{\exp(\frac{h\nu}{k_B T}) - 1} \tag{3.1}$$

which gives the temperature T dependent power per [unit area times solid angle times frequency]. In the case of the later used data set this would be in units of $[\frac{\mathrm{W}}{\mathrm{m}^2\,\mathrm{sr}\,\mathrm{Hz}}]$. In accordance with the used data set the formula

$$\nu I_\nu(\nu, T) = \frac{2h\nu^4}{c^2} \frac{1}{\exp(\frac{h\nu}{k_B T}) - 1} \tag{3.2}$$

in units of $[\frac{\mathrm{W}}{\mathrm{m}^2\,\mathrm{sr}}]$ will most commonly be used. Given the spectral radiance of a blackbody, it is rather trivial getting a formula for the associated photon density $n(\nu, T)$. For this, we multiply the $\nu I_\nu(\nu, T)$ by the factor $\frac{4\pi}{c}$ to obtain the energy density

$$\nu u(\nu, T) = \frac{8\pi h\nu^4}{c^3} \frac{1}{\exp(\frac{h\nu}{k_B T}) - 1} \tag{3.3}$$

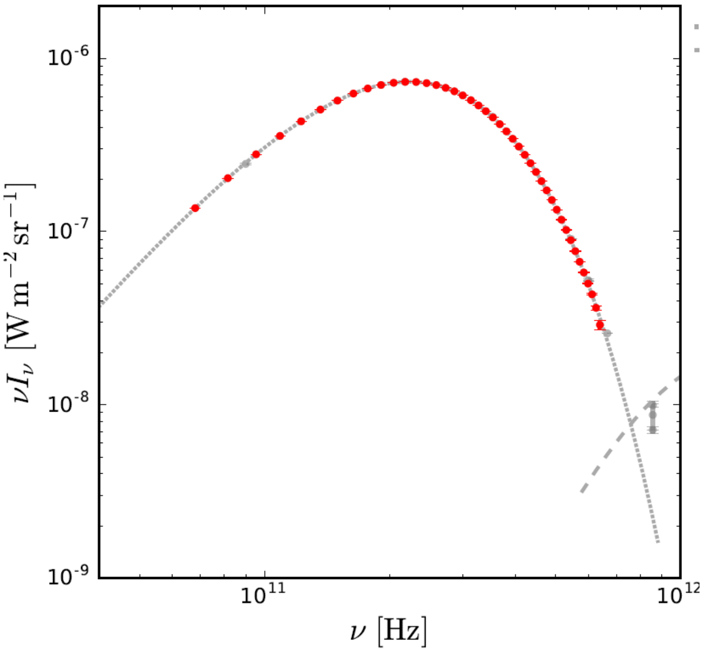

**Figure 3.1:** The graph shows the Cosmic Microwave Background data (red) fitted with a blackbody at T=2.7255 K and an amplitude of one (grey) (Hill et al, 2018).

and then divide by the energy of a photon emitted by the blackbody $\epsilon = h\nu$ to get to the photon density

$$\nu n(\nu, T) = \frac{8\pi\nu^3}{c^3}\frac{1}{\exp(\frac{h\nu}{k_B T}) - 1} \tag{3.4}$$

As said before, the CMB part of the spectrum is described by a single blackbody quite precisely, whereas the sources of the other parts of the spectrum are more complicated (Section 2.1) (Hill et al, 2018). The approach is to approximate the CPB spectrum with a sum of a sufficient amount of blackbodies. On the one hand this creates a model that stays comprehensible, while on the other hand the final fitted sum of blackbodies can always be deconstructed back into the singular blackbodies for ease of use.

As the CPB peaks in the CMB range and falls off towards both sides of the spectrum, further blackbodies used to describe other components of the spectrum will need a secondary parameter A, which is optimised for each spectral range.

## 3.2 Optimising decomposition of CPB

To finally fit a set of blackbodies, two arrays of starting values - priors - have to be determined for the needed number of blackbodies. To achieve this, the number of blackbodies is iteratively increased until the residuals of the spectral fit appear unstructured. This applies for 28 blackbodies for the spectrum seen in Figure 2.1. It fills the spectrum evenly, while not overfitting the dataset as much. The temperature for the CMB is set at 2.725 K for reference and the other 27 are then almost evenly spaced throughout the rest of the spectrum. As the low-energy end below the microwave frequency is far less important for the pair production, due to a lack of photon energy, there are only two blackbodies here around $10^{-2}\,K$ and $10^{-3}\,K$.

For the amplitudes $A_i$ starting points, values are estimated, which look visually reasonable, except for the CMB's amplitude which is set to one. Both sets of parameters $T_i$ and $A_i$ are viable for the model:

$$\sum_i A_i \cdot \nu I_{\nu,i}(\nu, T) = \sum_i \frac{2h\nu^4}{c^2} \frac{A_i}{\exp(\frac{h\nu}{k_B T_i}) - 1} \tag{3.5}$$

while the spectral fitting model $m$ is constructed of the form:

$$m = \sum_i K_i \frac{x^2}{\exp(\frac{x}{kT_i}) - 1} \tag{3.6}$$

with the photon energy $x = \epsilon = h\nu$, the $kT_i = k_B \cdot T_i$, which is a constant times the temperature times $k_B$ and $K_i = \frac{2}{c^2 h^3} A_i$, which is a constant times the amplitude.

For the first iteration of the fit, both the entirety of the temperatures and the amplitude of the CMB are kept fixed, so only the 27 amplitudes besides the CMB are fitted. For the uncertainty values in the used data set (Figure 2.1), the max-min values of the datapoints are used. This first iteration is to get better starting values for the amplitudes before fitting the entire model.

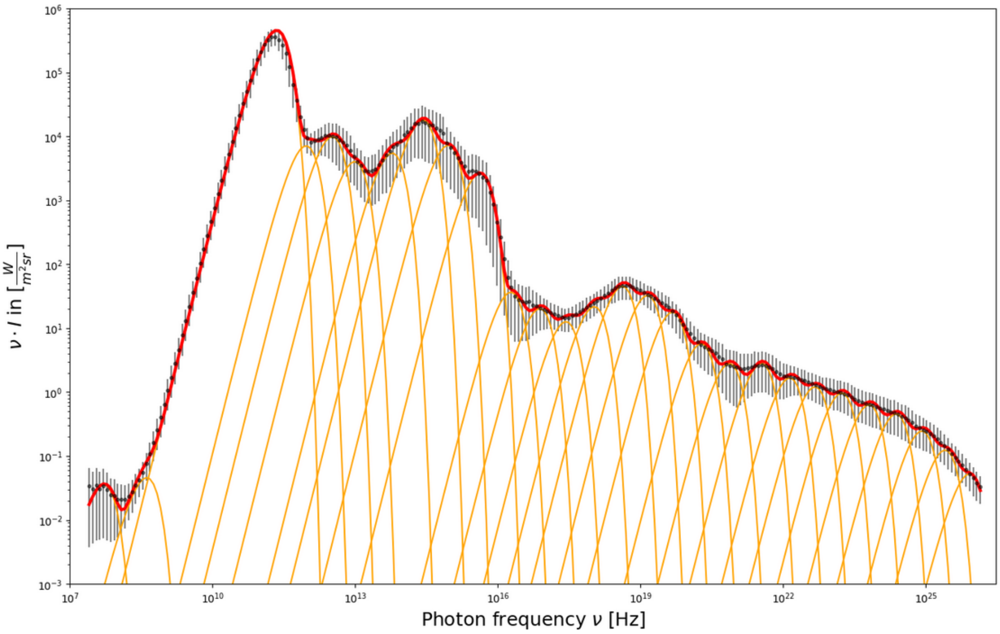

**Figure 3.2:** The figure shows the dataset Hill et al (2018) fitted with a sum of 28 blackbody with multiplicative scaling factors.

The result is then used in a second iteration, where both parameters of the CMB stay fixed, but the temperatures and amplitudes of all leftover blackbodies are fitted. Of course, this second iteration comes with far larger uncertainties for the parameters and covariances between pairs of amplitudes, pairs of temperatures and between temperatures and amplitudes. The final result of the fit used for the CPB can be seen in Figure 3.2.

# Chapter 4

# Pair production yield

With a model for the photon density of the CPB now determined, the next step is calculating the pair-production rate from the interaction of the photon fields with themselves. The most trivial formula describing this process is:

$$\dot{n} = c \cdot n_{ph}(\epsilon_1) \cdot n_{ph}(\epsilon_2) \cdot \sigma_{\epsilon_1\epsilon_2} \tag{4.1}$$

Here $n_{ph}(\epsilon_i)$ describes the photon density of an emitter (e.g. CPB, Sun, Earth, etc.) with photon energy $\epsilon_i$, c is the speed of light and $\sigma_{\epsilon_1\epsilon_2}$ is the cross section for the interaction of both photons, which in general is dependent on both energies and the collision angle. Therefore the cross section does not stay constant, but rather is calculated as follows (Siegert, 2023)

$$\sigma_{\gamma\gamma} = \frac{3\sigma_T}{16}(1-\beta^2) \cdot \left[(3-\beta^2)\ln\left(\frac{1+\beta}{1-\beta}\right) - 2\beta(2-\beta)^2\right] \tag{4.2}$$

$\sigma_T = 6.65 \cdot 10^{-25}\,\mathrm{cm}^2$ is the constant Thomson cross section and $\beta$ then describes the centre-of-momentum frame's (cm) relativistic velocity of the $e^-/e^+$ with

$$\beta = \sqrt{1 - \frac{2m_e^2c^4}{\epsilon_1\epsilon_2(1-\cos(\theta_\mu))}} \tag{4.3}$$

The cross section as a function of $2\epsilon_{\mathrm{cm}}^2$ is shown in Figure 4.1, where the maximum is at around $\sim \frac{\sigma_T}{4}$ and sharply rises as the two photons have enough combined energy to at least contribute double the electron resting energy of $2m_ec^2$ =1.022 MeV. As the resting energy of the electron/positron is an important reference here, it is defined as $E_0 = m_ec^2$ and all further photon energies are unitless and scaled by $\epsilon = \frac{h\nu}{E_0}$.
Two photons colliding in the laboratory system under the angle $\theta_\mu$ fulfil the Lorentz invariant scalar product (Böttcher & Schlickeiser, 1997)

$$\epsilon_1\epsilon_2(1 - cos\,\theta_\mu) = \epsilon_1\epsilon_2(1-\mu) = 2\epsilon_{cm}^2 \tag{4.4}$$

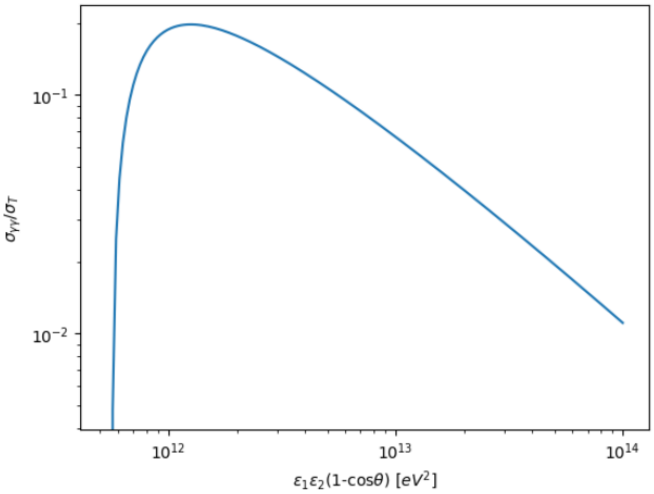

**Figure 4.1:** The figure shows the $\gamma\gamma$-cross section in units of Thomson cross sections in dependence of the photon energies in eV$^2$. The cross section has a sharp increase past the threshold of $\epsilon_1\epsilon_2(1-\cos\theta_\mu) = 2m_e^2c^4$ and it's maximum around $4m_e^2c^4$ at $\sim \frac{\sigma_T}{4}$.

The laboratory frame moves against the cm-frame with $\beta_c c$, while the produced electrons/positrons move with $\pm\beta_{cm}c$ in the cm-frame. Further, the corresponding Lorentz factors are calculated by (Böttcher & Schlickeiser, 1997):

$$\gamma_{c,cm} = \frac{1}{\sqrt{1-\beta_{c,cm}^2}} \tag{4.5}$$

What is of interest here, is the Lorentz factor of the electrons/positrons in the laboratory frame, which results from the following formula with $u$ being the cosine of the angle $\theta_u$ between $\beta_{cm}$ and $\beta_c$ (Böttcher & Schlickeiser, 1997):

$$\gamma_{\pm} = \gamma_{cm}\gamma_c(1 \pm \beta_{cm}\beta_c u) \tag{4.6}$$

After applying the conservation of energy in the form $\gamma_{cm} = \epsilon_{cm}$, the angle u between $\beta_c$ and $\beta_{cm}$ becomes fixed to:

$$u = u_0 = \frac{E - 2\gamma_-}{\beta_{cm}N} \tag{4.7}$$

with the sum of energies $E = \epsilon_1 + \epsilon_2$ and the term $N = \sqrt{E^2 - 4\epsilon_{cm}^2}$. After all angles are determined, the differential yield of electron-positron pairs is given by (Böttcher & Schlickeiser, 1997):

$$\dot{n}(\gamma_-) = \frac{c}{4}\int_0^\infty d\epsilon_1\, n_{ph}(\epsilon_1)\int_{\epsilon_2^L}^\infty d\epsilon_2\, n_{ph}(\epsilon_2)\cdot\cdot\int_{-1}^{1-\frac{2}{\epsilon_1\epsilon_2}} d\mu(1-\mu)\frac{d\sigma}{d\gamma_-} \tag{4.8}$$

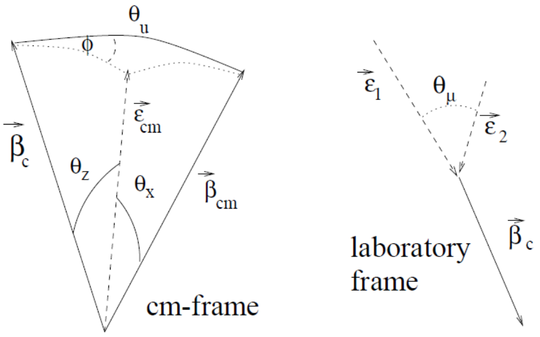

**Figure 4.2:** Sketch of the photon-photon collision in the laboratory frame and centre-of-momentum (cm) frame. $\beta_c$ describes the relative motion of both frames of reference. Meanwhile $\beta_{cm}$ characterizes the motion of the produced electrons and positrons (Böttcher & Schlickeiser, 1997).

with $\epsilon_2^L$ being the lower limit $\epsilon_2^L = \max\{\frac{1}{\epsilon_1}, \gamma_- + 1 - \epsilon_1\}$ and $\mu = cos\,\theta_\mu$. The differential cross section $\frac{d\sigma}{d\gamma_-}$ is defined as follows:

$$\frac{d\sigma}{d\gamma_-} = \oint d\Omega_{cm} \frac{d^2\sigma}{d\Omega_{cm} d\gamma_{cm}} \frac{d\gamma_{cm}}{d\gamma_-} \tag{4.9}$$

After further, purely algebraic steps to calculate the differential cross section, the final form of the differential pair yield integral is (Böttcher & Schlickeiser, 1997):

$$\dot{n}(\gamma_-) = \frac{3}{4}\sigma_T c \cdot \int\limits_0^\infty d\epsilon_1 \frac{n_{ph}(\epsilon_1)}{\epsilon_1^2} \int\limits_{\epsilon_2^L}^\infty d\epsilon_2 \frac{n_{ph}(\epsilon_2)}{\epsilon_2^2} \left\{ \frac{\sqrt{E^2 - 4\epsilon_{cm}^2}}{4} + H_+(\epsilon_1, \epsilon_2) + H_-(\epsilon_1, \epsilon_2) \right\} \Bigg|_{\epsilon_{cm}^L}^{\epsilon_{cm}^U} \tag{4.10}$$

$H_\pm(\epsilon_1, \epsilon_2)$ are auxiliary functions, that - once unravelled - depend on the photon energies $\epsilon_{1,2}$ over which is integrated, $\epsilon_{cm}$ where the limits $\epsilon_{cm}^L$ and $\epsilon_{cm}^U$ are plugged in and $\gamma_-$ which is the variable of the differential pair yield. The $\epsilon_{cm}$ limits are defined as follows (Böttcher & Schlickeiser, 1997):

$$\epsilon_{cm}^L = \max\left\{1, \epsilon_{cm}^\dagger\right\} \tag{4.11}$$

$$\epsilon_{cm}^U = \min\left\{\sqrt{\epsilon_1\epsilon_2}, \epsilon_{cm}^*\right\} \tag{4.12}$$

with

$$\left(\epsilon_{cm}^{*,\dagger}\right)^2 = \frac{1}{2}\left(\gamma_-[E - \gamma_-] + 1 \pm \sqrt{(\gamma_-[E - \gamma_-] + 1)^2 - E^2}\right) \tag{4.13}$$

The integral (4.10) is finally integrated via the composite 1/3 Simpson‘s rule. The Simpson‘s 1/3 rule, or just Simpson‘s rule, is an improvement upon the simple trapezoidal rule for numerical integration. A function $f(x)$ is approximated in the interval $[a, b]$ with a quadratic interpolating polynomial $p_2(f)$ and the parameter $c = ((a + b)/2)$ (Atkinson, 1989):

$$I_2(f) = \int_a^b \left[ \frac{(x-c)(x-b)}{(a-c)(a-b)} f(a) + \frac{(x-a)(x-b)}{(c-a)(c-b)} f(c) + \frac{(x-a)(x-c)}{(b-a)(b-c)} f(b) \right] dx \tag{4.14}$$

which integrated results in:

$$I_2(f) = \frac{h}{3} \left[ f(a) + 4f\Big(\frac{a+b}{2}\Big) + f(b) \right] \quad \text{with} \quad h = \frac{b-a}{2} \tag{4.15}$$

For n equal subdivisions of $[a, b]$, the composite Simpson‘s 1/3 rule is achieved. In this case values inside the interval are weighted with alternating weights of 2/3 and 4/3. The asymptotic error $E_n(f)$ of this rule is then (Atkinson, 1989):

$$E_n(f) = -\frac{h^4}{180}[f^{(3)}(b) - f^{(3)}(a)] \tag{4.16}$$

To apply the rule, the photon densities are decomposed into the singular blackbodies again. The energy range over which is integrated, is split into discrete values $E_{\text{bounds}}$, evenly spaced along the logarithmic scale, defined by a maximum photon energy, minimum photon energy and a number of discrete values $N_E$. The arithmetic average of these discrete energy values $E_{bounds}$ makes up an array of photon energies for integration $E_{cen}$, while the difference of the values in $E_{bounds}$ makes up an array of energy step widths $E_{wid}$. To go along with the model, all energies are divided by $E_0$ to make them unitless. With respect to the minimum energy $\epsilon_2^L$ necessary for energy conservation in equation (4.10), the integrand (4.17) is calculated for every combination $(n, m)$ of values in $E_{cen}$ for both photon densities, while every value of the integrand is then multiplied by both the respective values from $E_{wid}$ (4.18).

$$f_{nm}(T_i, T_j) = \frac{3}{4}\sigma_T c \frac{n_{ph}(\epsilon_n, T_i)}{\epsilon_n^2} \frac{n_{ph}(\epsilon_m, T_j)}{\epsilon_m^2} \cdot \left\{ \frac{\sqrt{E^2 - 4\epsilon_{cm}^2}}{4} + H_+(\epsilon_n, \epsilon_m) + H_-(\epsilon_n, \epsilon_m) \right\} \Bigg|_{\epsilon_{cm}^L}^{\epsilon_{cm}^U} \tag{4.17}$$

The integrand values are then further weighted by alternating factors of $\frac{4}{3}$ and $\frac{2}{3}$, called $w_{\epsilon_n}$ and $w_{\epsilon_m}$ below, except for the first and last. This gives the result of the integral for one combination of blackbodies $(i, j)$ and a singular value of $\gamma_-$ the form:

$$\sum_{nm} w_{\epsilon_n} \cdot w_{\epsilon_m} \cdot f_{nm}(T_i, T_j) \cdot E_{wid_n} \cdot E_{wid_m} \tag{4.18}$$

$f_{nm}(T_i, T_j)$ is the value of the integrand for one pair of energies $n$ and $m$ and a combination of blackbodies $(i, j)$, $E_{wid_n}$ and $E_{wid_m}$ are the energy step widths and the weights $w_{\epsilon_n}$ and $w_{\epsilon_m}$. Sum (4.18) is repeated for all combinations of blackbodies $(i, j)$ and every sum is further weighted with the corresponding amplitudes $A_i$ and $A_j$.

Furthermore the sum of all blackbody combinations $(i, j)$ has to be repeated for an array of $\gamma_-$ values to get an actual spectrum. Combinations $(i, j)$ that do not exceed a certain energy threshold are skipped in the calculation. The threshold is given by the following with the indices 1 and 2 differentiating between the different photon densities in the integral and not different components of the same photon density:

$$\log_{10}(k_B T_1) + \log_{10}(k_B T_2) > 6 \tag{4.19}$$

The final result is an array of 28 rows for all fitted blackbodies and 28 columns for the same 28 blackbodies. All cells of this array contain 200 positron production values for all calculated 200 $\gamma_-$values. The final results in the array have to then be multiplied by $E_0^2$ to arrive at the unit of the pair production rate $\left[\frac{\mathrm{e}^{\pm}}{\mathrm{s\,cm^3}}\right]$. Consider one last step: For every combination of blackbodies $(i, j)$ describing different components of the CPB, the final array will always have the symmetrical counterpart $(j, i)$. So the array basically counts any positron yield, where $i \neq j$ double, which does not match the idea of only one instance of a CPB. Therefore, for any given blackbody combination $(i, j)$ in the final array, the symmetrical counterpart $(j, i)$ is taken out.

To now calculate the uncertainty of the result, consider the following: The integral can be described as follows:

$$q_{ijk} = I_{ijk} A_i A_j \tag{4.20}$$

where $q_{ijk}$ is one element of the output array from the above integral for amplitude combination $A_i$, $A_j$ and $\gamma_-$ step $k$ with $I_{ijk}$ being the same value, only before multiplication with the corresponding amplitudes, to simplify the calculation a bit. So $I_{ijk}$ is dependent on both temperatures $T_i$ and $T_j$ but not on the amplitudes. To sum the values $q_{ijk}$ for a given $\gamma$ value k over all blackbody combinations, the equation is:

$$E_0^2 s_k = E_0^2 \sum_{i,j} I_{ijk} A_i A_j = E_0^2 \sum_i A_i \left( \sum_j I_{ijk} A_j \right) \tag{4.21}$$

The array of values $s_k$ produces the data points seen in Figure 5.1. Using (4.21), Gaussian error propagation yields:

$$\begin{aligned} E_0^2 \sigma_{s_k} =& E_0^2 \Bigg[ \sum_i \sigma_{A_i}^2 \left(\frac{\partial s_k}{\partial A_i}\right)^2 + \sum_j \sigma_{A_j}^2 \left(\frac{\partial s_k}{\partial A_j}\right)^2 + \sum_i \sigma_{T_i}^2 \left(\frac{\partial s_k}{\partial T_i}\right)^2 + \sum_j \sigma_{T_j}^2 \left(\frac{\partial s_k}{\partial T_j}\right)^2 \\ &+ 2 \sum_{i,j\neq i} \left[\frac{\partial s_k}{\partial T_i}\frac{\partial s_k}{\partial T_j}\sigma_{T_i T_j} + \frac{\partial s_k}{\partial A_i}\frac{\partial s_k}{\partial A_j}\sigma_{A_i A_j}\right] + 2 \sum_{i,j} \left[\frac{\partial s_k}{\partial T_i}\frac{\partial s_k}{\partial A_i}\sigma_{T_i A_i} + \frac{\partial s_k}{\partial T_j}\frac{\partial s_k}{\partial A_j}\sigma_{T_j A_j} \right. \\ &\left. \left. + \frac{\partial s_k}{\partial T_i}\frac{\partial s_k}{\partial A_j}\sigma_{T_i A_j} + \frac{\partial s_k}{\partial A_i}\frac{\partial s_k}{\partial T_j}\sigma_{A_i T_j}\right]\right]^{1/2} \end{aligned} \tag{4.22}$$

using the covariance values $\sigma_{T_iT_j}$, $\sigma_{A_iA_j}$, $\sigma_{T_iA_j}$ and all variations. The partial derivatives $\frac{\partial s_k}{\partial A_i}$ are given by:

$$\frac{\partial s_k}{\partial A_i} = \sum_j I_{ijk} A_j \quad \text{and} \quad \frac{\partial s_k}{\partial A_j} = \sum_i I_{ijk} A_i \tag{4.23}$$

The uncertainties of $s_k$ not only depend on $\sigma_{A_{i,j}}$, but also on the temperatures uncertainties $\sigma_{T_{i,j}}$ and all the covariance terms. For the derivatives of the temperature, $I_{ijk}$ takes the form seen in eq. 4.18, where $f_{mn}$ is the temperature dependent integrand. Therefore the following derivatives will be needed:

$$\frac{\partial I_{ijk}}{\partial T_i} = \sum_{m,n} \sigma_{\epsilon_m} \sigma_{\epsilon_n} d\epsilon_m d\epsilon_n \frac{\partial f_{mn}}{\partial T_i} \quad \text{and} \quad \frac{\partial I_{ijk}}{\partial T_j} = \sum_{m,n} \sigma_{\epsilon_m} \sigma_{\epsilon_n} d\epsilon_m d\epsilon_n \frac{\partial f_{mn}}{\partial T_j} \tag{4.24}$$

where the derivatives $\frac{\partial f_{mn}}{\partial T_i}$ and $\frac{\partial f_{mn}}{\partial T_j}$ is:

$$\frac{\partial f_{mn}}{\partial T_{i,j}} = \frac{3}{4} \sigma_T c \frac{1}{\epsilon_m^2} \frac{1}{\epsilon_n^2} \cdot \frac{\partial}{\partial T_{i,j}} \left( n_{T_i}(\epsilon_m) n_{T_j}(\epsilon_n) \right) \cdot \left\{ \frac{\sqrt{E^2 - 4\epsilon_{cm}^2}}{4} + H_+ + H_- \right\} \Bigg|_{\epsilon_{cm}^L}^{\epsilon_{cm}^U} \tag{4.25}$$

which is just (4.17) with the derivative of the product of photon densities.
All these derivatives are necessary to finally determine:

$$\frac{\partial s_k}{\partial T_i} = \sum_j A_i A_j \frac{\partial I_{ijk}}{\partial T_i} \quad \text{and} \quad \frac{\partial s_k}{\partial T_j} = \sum_i A_i A_j \frac{\partial I_{ijk}}{\partial T_j} \tag{4.26}$$

The full injection rate $Q$ is finally determined via:

$$E_0^2 Q = E_0^2 \sum_k s_k \cdot w_k = E_0^2 \sum_k w_k \left( \sum_i A_i \left( \sum_j I_{ijk} A_j \right) \right) \tag{4.27}$$

with $w_k$ being the $\gamma$-step widths of a given value $s_k$ (from $E_{wid}$). Similarly to (4.22), the uncertainties of Q is calculated by:

$$\begin{aligned} E_0^2 \sigma_Q = & E_0^2 \Bigg[ \sum_i \sigma_{A_i}^2 \left( \frac{\partial Q}{\partial A_i} \right)^2 + \sum_j \sigma_{A_j}^2 \left( \frac{\partial Q}{\partial A_j} \right)^2 + \sum_i \sigma_{T_i}^2 \left( \frac{\partial Q}{\partial T_i} \right)^2 + \sum_j \sigma_{T_j}^2 \left( \frac{\partial Q}{\partial T_j} \right)^2 \\ & + 2 \sum_{i,j \neq i} \left[ \frac{\partial Q}{\partial T_i} \frac{\partial Q}{\partial T_j} \sigma_{T_iT_j} + \frac{\partial Q}{\partial A_i} \frac{\partial Q}{\partial A_j} \sigma_{A_iA_j} \right] + 2 \sum_{i,j} \left[ \frac{\partial Q}{\partial T_i} \frac{\partial Q}{\partial A_i} \sigma_{T_iA_i} + \frac{\partial Q}{\partial T_j} \frac{\partial Q}{\partial A_j} \sigma_{T_jA_j} \right. \\ & \left. \left. + \frac{\partial Q}{\partial T_i} \frac{\partial Q}{\partial A_j} \sigma_{T_iA_j} + \frac{\partial Q}{\partial A_i} \frac{\partial Q}{\partial T_j} \sigma_{A_iT_j} \right] \right]^{1/2} \end{aligned} \tag{4.28}$$

with the derivatives:

$$\frac{\partial Q}{\partial A_i} = \sum_k w_k \left[ \sum_j I_{ijk} A_j \right] \quad \text{and} \quad \frac{\partial Q}{\partial A_j} = \sum_k w_k \left[ \sum_i I_{ijk} A_i \right] \tag{4.29}$$

$$\frac{\partial Q}{\partial T_i} = \sum_k w_k \left[ A_i \sum_j A_j \frac{\partial I_{ijk}}{\partial T_i} \right] \quad \text{and} \quad \frac{\partial Q}{\partial T_j} = \sum_k w_k \left[ A_j \sum_j A_i \frac{\partial I_{ijk}}{\partial T_j} \right] \tag{4.30}$$

With the method of integration in place, the second photon density in the integral (4.10) can now be substituted by all kinds of photon densities from different sources interacting with the CPB, like the earth, sun or Milky Way for example.

# Chapter 5

# Pair production rates

The following shows the results from the yield integral (4.10) calculated with both photon densities being the CPB. Furthermore, the planets and Sun of the solar system are used as photon emitters interacting with the CPB, to gauge the importance of these positron contributions. For these finite bodies as emitters, luminosities and fluxes are further calculated with line-of-sight (LOS) integration. Lastly an estimate is made for the injection rate of positrons produced by the Milky Ways infrared to UV radiation, to see how its order of magnitude compares to that of the CPB.

## 5.1 Interaction of the CPB with itself

To bring the results of the integral (4.10) into a visually usable form, the values from all blackbody combinations for any given $\gamma$ value are summed as seen in (4.21), the results of which can be seen in Figure 5.1.

It appears that most of the positrons created, possess relatively little kinetic energy, as the injection rate of positrons falls monotonously from $\gamma = 1$ to about $\gamma = 3 \cdot 10^3$ with a powerlaw index of roughly $-1$ (see Table 5.2). Beyond this point the injection rate increases by roughly a single order of magnitude, before eventually falling off completely. Now to look at some more specific examples of what the integral produces for the CPB interacting with itself. For this, the spectral positron yields of some of the blackbodies interacting with the highest energy CGB blackbody are portrayed in Figure 5.2. The examples start with the infrared, as no lower-energy blackbodies yield any positrons. Even for the infrared, the yield is of many orders of magnitude smaller, than any other example. Furthermore, the yield only covers a small range of high-energy positrons ($\gamma = 10^6 - 10^7$). The greatest magnitude of yield is achieved by the CGB interacting with the optical range of the CPB within these examples. Compared to Figure 5.1, the orange curve, seems to heavily contribute to the increase in the higher energy range. The combination with the

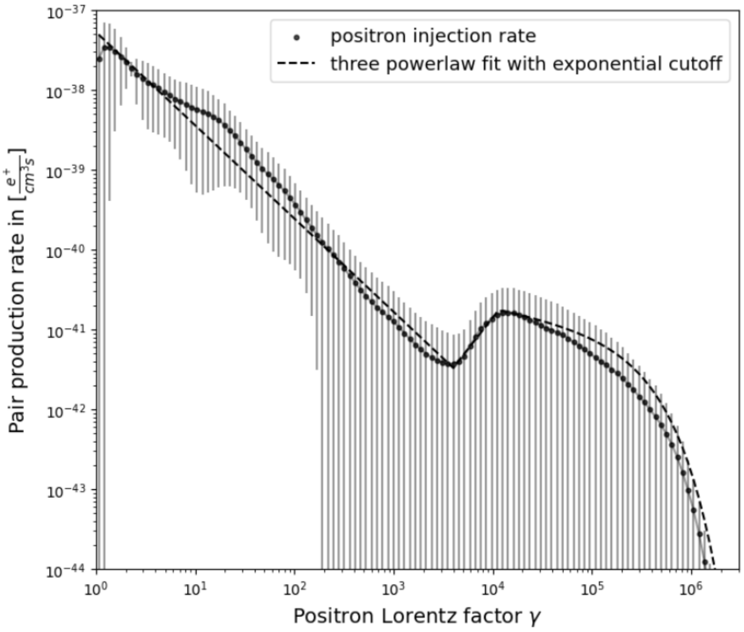

**Figure 5.1:** The plot shows the summed curves following (4.21) with error bars, that might be overestimated at higher energies, due to the decomposition into blackbodies. The dashed line is a fitted triple powerlaw function with exponential cutoff.

optical blackbody also creates positrons with a larger energy coverage, down to $\gamma \approx 10^2$. From the optical onwards, the magnitude of positron yields decreases again, but they all cover a large energy range of positrons, basically $\gamma = 1 - 10^7$.

For another example, the combinations of all same blackbodies can be examined in Figure 5.3, meaning the various components of the CPB, as decomposed here, interacting with themselves. Analysing Figure 5.3, the first thing to note, is that only the CXB and CGB components of the CPB can interact with themselves to create positrons, as all the others do not possess photons with enough energy to reach the threshold. Moving from the CXB upwards in photon energy increases the maximum of positron yields up to the transition between CXB and CGB, from where on it continues downwards, most likely as the cross section decrease for the higher energy combinations. On the other hand however, moving up in photon energy extends the energy range over which the positrons are created, up to the highest combination, as can also be seen in Figure 5.2.

Looking at which combinations of blackbodies contribute the highest positron production rate, the three most relevant pairs starting from the top are (8, 28), (9, 27) and (10, 26). Each of these pairs is responsible for roughly 17 % of the total injection rate across the spectrum respectively. According to this, a large amount of the produced positrons are the products of high-energy $\gamma$-ray photons towards the end of the CPB spectrum interacting with photons from the optical to ultraviolet background radiation. Looking at Figure 5.4, the positrons from these combinations are of higher energy, mainly around the increasing

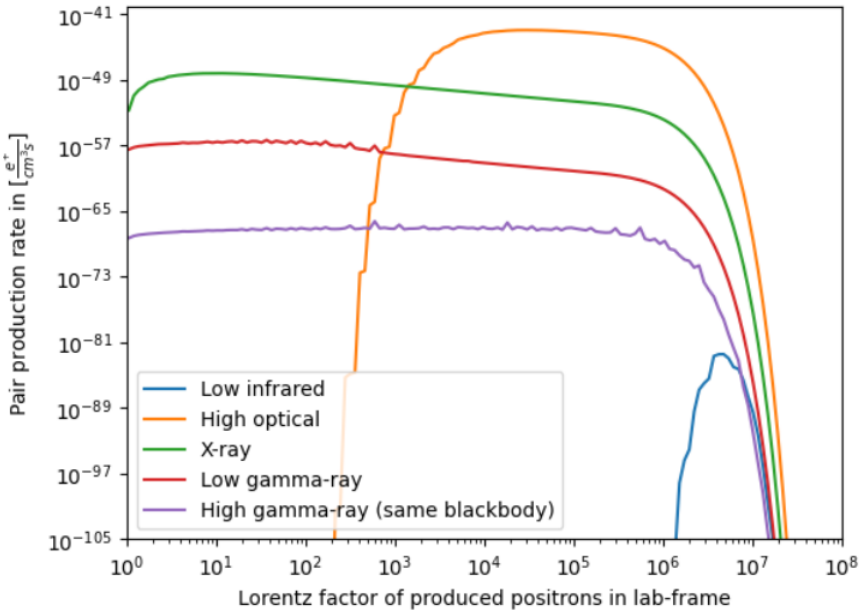

**Figure 5.2:** The above shows the spectral positron yields of some exemplary blackbodies of the CPB reacting with the highest energy CGB blackbody. The examples start with the infrared, as lower-energy components do not create positrons in this combination.

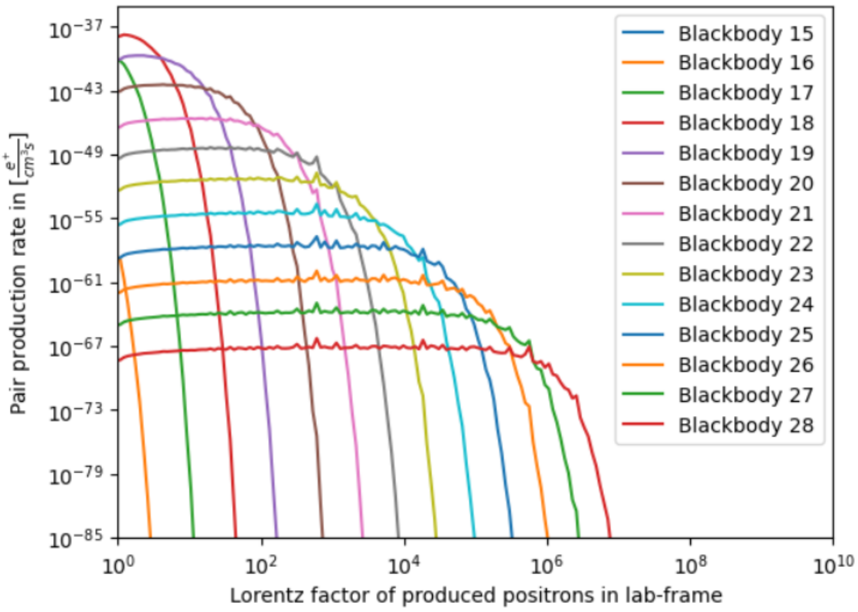

**Figure 5.3:** The above shows the spectral positron yields of all (that yield anything) blackbodies interacting with themselves. Blackbodies 15-18 correspond to about the CXB range and any above to the CGB range.

| Blackbody combination | Positron injection rate $\left[\frac{e^+}{cm^3 s}\right]$ |
|---|---|
| (8,28) | $3.60 \cdot 10^{-37}$ |
| (9,27) | $3.55 \cdot 10^{-37}$ |
| (10,26) | $3.52 \cdot 10^{-37}$ |

**Table 5.1:** Total positron injection rate of of three blackbody combinations with the greatest contributions towards the total.

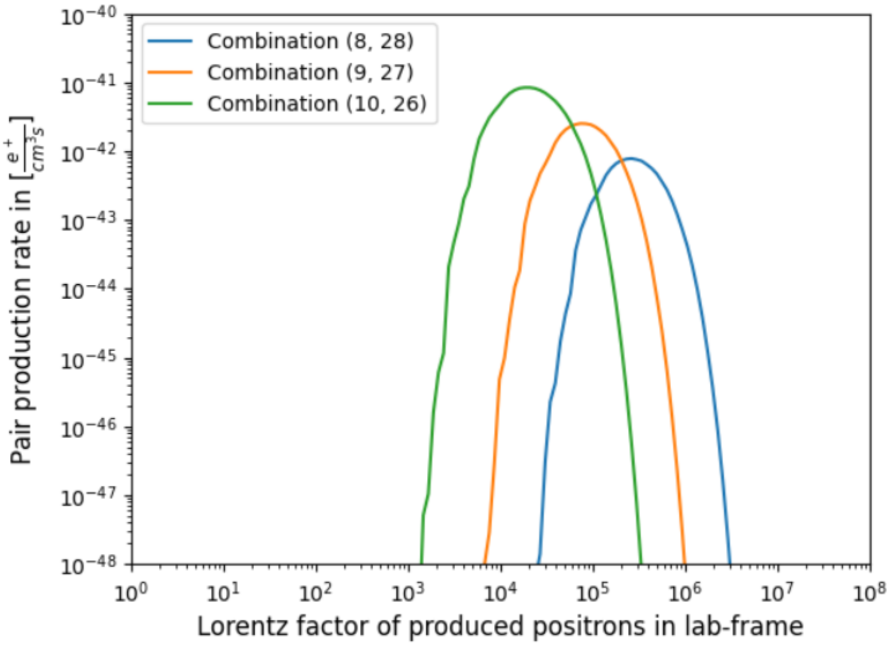

**Figure 5.4:** Plotted is the spectral positron injection rate of the of the three blackbody combinations in Table 5.1. These blackbody yield high-energy positrons, explaining the sudden increase in Figure 5.1.

section of Figure 5.1, possibly explaining the break in the monotonous falloff. Considering section 2.1, it has to be mentioned, that especially the CUB and COB sections of the CPB, are rather difficult to measure precisely, which introduces more uncertainty as for example contributions by the CMB component would. Therefore finding better methods to measure the COB and CUB components or improving existing methods would significantly aid the more precise calculation of CPB created positrons.

The resulting data in Figure 5.1 is fitted with a function for ease of use in later diffusion calculations. The function is a piece-wise function of three powerlaws with an exponential cutoff in the end of the form:

$$Q_1(x) = f_1(x)\Theta(z_1 - x) + f_2(x)\Theta(x - z_1)\Theta(z_2 - x) + f_3(x)\Theta(x - z_2) \tag{5.1}$$

$\Theta(x)$ is the Heaviside step function with the $z_1$ and $z_2$ being the intersection point of two neighbouring powerlaws. The variable $x$ is the Lorentz factor $\gamma$ of the positrons. The powerlaws are defined as follows:

$$f_1(x) = f_2(x) = a_{1,2}x^{b_{1,2}} \tag{5.2}$$

$$f_3(x) = a_3 x^{b_3} e^{-x/c_3} \tag{5.3}$$

The parameters are fitted with `iminuit` similarly to the CPB in section 3.2. The results can be found in Table 5.2.

| Parameter | Value |
|---|---|
| $a_1$ | $(5.3 \pm 0.5) \cdot 10^{-38}\,\frac{\mathrm{e}^+}{\mathrm{cm}^3\mathrm{s}}$ |
| $b_1$ | $(-1.16 \pm 0.03)$ |
| $a_2$ | $(0.6 \pm 1.9) \cdot 10^{-47}\,\frac{\mathrm{e}^+}{\mathrm{cm}^3\mathrm{s}}$ |
| $b_2$ | $(1.5 \pm 0.2)$ |
| $a_3$ | $(1.9 \pm 0.3) \cdot 10^{-40}\,\frac{\mathrm{e}^+}{\mathrm{cm}^3\mathrm{s}}$ |
| $b_3$ | $(-2.4 \pm 0.5) \cdot 10^{-1}$ |
| $c_3$ | $(1.737 \pm 0.005) \cdot 10^5$ |
| $z_1$ | $(4.4 \pm 0.7) \cdot 10^3$ |
| $z_2$ | $(1.1 \pm 0.7) \cdot 10^4$ |

**Table 5.2:** Set of parameters fitted to a three powerlaw function with exponential cutoff, used to approximate the CPB positron yield spectrum. The uncertainties of the parameters come from the fit to the spectrum the approximate uncertainties of the blackbody decomposition.

In the following two sections, similar results are estimated for the CPBs radiation interacting with the Solar System‘s radiation and the Milky Way‘s IR-UV radiation, to compare their output of positrons. To help with this, the results in Figure 5.1 can be summed over the energy spectrum as seen in (4.27), finally arriving at a total, constant injection rate of $Q_{\mathrm{CPB}} = (2.0 \pm 0.5) \cdot 10^{-36}\,\frac{\mathrm{e}^+}{\mathrm{cm}^3\mathrm{s}}$. Note that, despite the unit being $\left[\frac{\mathrm{e}^+}{\mathrm{cm}^3\mathrm{s}}\right]$, the same amount of electrons are injected.

Now let the Milky Way have a visible annihilation rate of $\sim 5 \cdot 10^{43}\,\frac{\mathrm{e}^+}{\mathrm{s}}$ (Siegert, 2023) and consider it a disk with an estimated diameter of $10^5$ ly and a thickness of $10^3$ ly. This gives a volume of $V_{\mathrm{MW}} = 1.6 \cdot 10^{66}\,\mathrm{cm}^3$. Now to gauge the magnitude of $Q_{\mathrm{CPB}}$, imagine the $V_{\mathrm{MW}}$ to only have positrons contributed by the CPB. This gives a injection rate of $\sim 3.2 \cdot 10^{30}\,\frac{\mathrm{e}^+}{\mathrm{s}}$. So assuming all positrons injected into this volume annihilated visibly, the CPB‘s annihilation rate is not even close to that of the Milky Way by the order of $10^{13}$. To arrive at the order of magnitude of the Milky Way‘s visible annihilation rate, the CPB‘s injection would therefore need to fill a volume of approximately $10^{13}$ times the volume of the Milky Way or in other words a spherical volume with a radius of $\sim 58$ Mpc.

This is just a rough estimate of the 511 keV contribution of the CPB, which is going to be expanded upon in chapter 6.

Beyond that, the actual result of interest is how many 511 keV photons the created positrons can supply via electron-positron annihilation. For this, section 6 will be using the above parameters (Table 5.2) to calculate the positrons diffusion through the IGM and their inevitable annihilation yields.

## 5.2 Interaction of the CPB with the IR, optical, UV spectra of the Solar System

For the following, the contributions to positron production from the larger bodies of our Solar System are analysed. For this, the emitting bodies are approximated as blackbody emitters, with a set temperature. The Sun is set to be $T_s = 5800\,\mathrm{K}$ as a basis, while the temperatures of the other planets are estimated with a simple equation of blackbody emission and absorption between the sun and the corresponding planet:

$$T_p = T_s \left( (1 - a_p)^{1/2} \frac{R_s}{2D_p} \right)^{1/2} \tag{5.4}$$

The temperature of the planet $T_p$ is calculated with the planets Bond albedo value $a_p$ and its average distance to the sun $D_p$, with the Sun‘s radius being $R_s$ [1]. The integral (4.10) is used, where one of the photon densities is changed to the bodies blackbody and the number of $\gamma$ steps is increased resulting in a [28 itmes 1 times 1000] array of values. Summing all the values is done as described in section 4 producing a total injection rate of the solar system body $q_p$.

The problem that arises in this case, is the calculated injection rate, which is only constant on the immediate surface of the emitting body, as the emitted photon density decreases with the square of distance. As such the emissivity of any of the considered bodies gains the form $\epsilon_p(r) = q_p \left(\frac{R_s}{r}\right)^2$ with the suns radius $R_s$ and the distance from the centre of the body to the earth $r$. Any value for $r$ smaller than $R_s$ is considered to be $R_s$ for further calculations as to avoid singularities.

The flux of positrons along a sight line is calculated via:

$$F_p = \frac{1}{4\pi\, sr} \int_0^R ds\, \epsilon_p(s) \tag{5.5}$$

---

[1] Basic data about the planets for these calculations are taken from their respective Planetary fact sheets: `https://nssdc.gsfc.nasa.gov/planetary/factsheet/`.

where $s$ describes the line of sight as up to a maximum distance of $R$:

$$\vec{s} = \begin{pmatrix} x_0 \\ y_0 \\ z_0 \end{pmatrix} + s \cdot \begin{pmatrix} \cos\phi \cos\theta \\ \sin\phi \cos\theta \\ \sin\theta \end{pmatrix} \tag{5.6}$$

with the position of the observer $\vec{s}_0$, the direction of the sight line in the second vector and the distance along this line $s$ (Siegert, 2024). The luminosity is then given by:

$$L_p = \int_{4\pi} d\Omega \int_0^R ds\, s^2 \epsilon_p(s) \tag{5.7}$$

Most of the calculations are done with the tool provided in Siegert (2024). For the distance between the observer (Earth) and the other planets the distance between said planet and the Sun is used as an average of the maximum and minimum distance between the Earth and said planet. The upper limit of both above integrals is set to be $R = 100\,\mathrm{AU}$. As an exception, the integrals for earth are calculated by hand, as both the position of the emitter and observer are the same, reducing the integrals to:

$$F_e = \frac{q_p}{4\pi\, sr} \int_0^R ds \left(\frac{R_s}{s}\right)^2 \tag{5.8}$$

$$L_e = 4\pi q_p R_s^2 \int_0^R ds \tag{5.9}$$

The fluxes and luminosities can be found below in Table 5.3:
To now compare magnitudes with the CPBs positron production, the flux and luminosity can be calculated with (5.5) and (5.6). The emissivity is substituted by the constant injection rate $Q$ producing the flux $F_{CPB} = 2.41 \cdot 10^{-22}\, \frac{\mathrm{e}^+}{\mathrm{cm}^2 \mathrm{s}\, \mathrm{sr}}$ and the luminosity $L_{CPB} = 2.83 \cdot 10^{10}\, s^{-1}$. Compared to the Table 5.3, the CPB seems to outshine the planets of the solar system by at least some orders of magnitude, while the Sun on the other hand outshines the CPB by many orders of magnitude itself. However, when the spectral positron injection rate of the solar system is displayed in Figure 5.5, it is easy to spot, that the created positrons only begin at energy values of $\gamma \sim 3 \cdot 10^3$.
As will become apparent later, after calculating diffusion times and annihilation times, only low-energy positrons are viable for the creation of 511 keV photons without the consideration of cosmology. Therefore the CPB outshines the solar systems low-energy positrons by magnitudes.
Note that only IR, optical and UV spectra are considered in the above. This means, other blackbody combinations with the CPB, as for example the $\gamma-$ray emissions from the Sun

| Body | Flux $\left[\frac{\mathrm{e}^+}{\mathrm{cm}^2\,\mathrm{s}\,\mathrm{sr}}\right]$ | Luminosity $\left[\frac{\mathrm{e}^+}{\mathrm{s}}\right]$ |
|---|---|---|
| Sun | $2.72 \cdot 10^{-10}$ | $4.04 \cdot 10^{16}$ |
| Mercury | $1.15 \cdot 10^{-25}$ | $8.06 \cdot 10^{3}$ |
| Venus | $4.94 \cdot 10^{-28}$ | $1.53 \cdot 10^{1}$ |
| Earth | $5.39 \cdot 10^{-24}$ | $7.47 \cdot 10^{1}$ |
| Mars | $2.18 \cdot 10^{-29}$ | $1.30$ |
| Jupiter | $5.30 \cdot 10^{-33}$ | $2.61 \cdot 10^{-3}$ |
| Saturn | $1.19 \cdot 10^{-35}$ | $1.22 \cdot 10^{-5}$ |
| Uranus | $2.32 \cdot 10^{-40}$ | $5.18 \cdot 10^{-10}$ |
| Neptune | $2.58 \cdot 10^{-43}$ | $9.48 \cdot 10^{-13}$ |

**Table 5.3:** Calculated are the fluxes of positrons created by the blackbody radiation of a the corresponding body interacting with the CPB across a line of sight out to 100 AU and the luminosity of the same with the earth as the observer position.

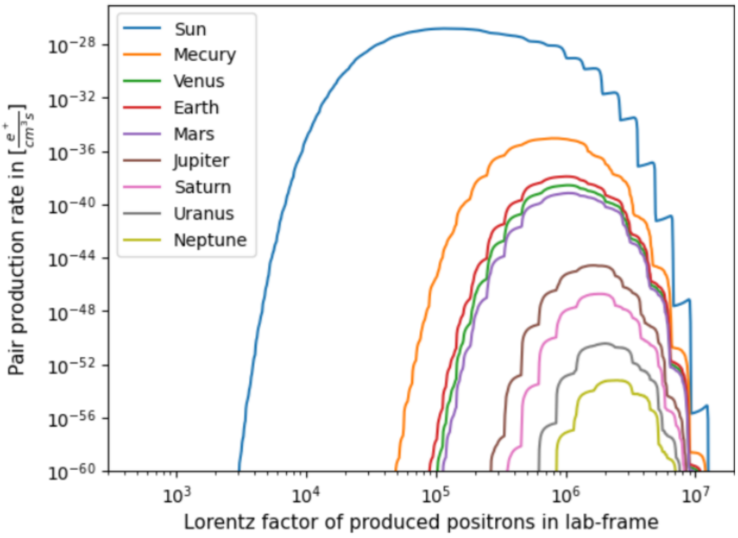

**Figure 5.5:** The summed spectral injection rate of solar system bodies is shown above. All values are from the direct surface of the corresponding body.

or Earth are neglected, although these might also make considerable contributions. The values in Table 5.3 are therefore to be taken as lower limits. Positrons emitted by the Sun for example might make a significant contribution to the 511 keV line, as the dense photon field from the Sun close to it‘s surface could quickly cool positrons, making them viable for annihilation.

## 5.3 Interaction of the CPB with the IR, optical, UV spectrum of the Milky Way

To have a look at the positron production via the interaction of the CPB photons with the IR, optical and UV radiation from the Milky Way, the following model by Cirelli & Panci (2009) in Figure 5.6 is used.

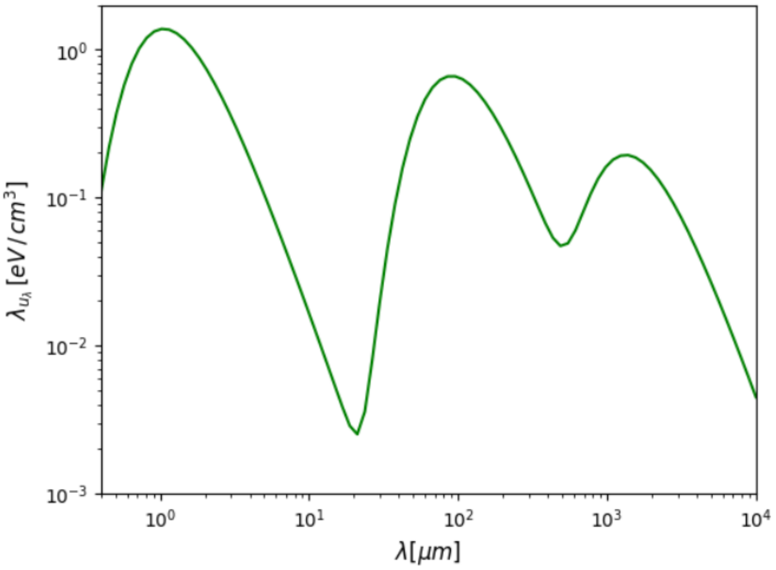

**Figure 5.6:** Milky Way model made up of three blackbodies for starlight, infrared and CMB emissions (from left to right) (Cirelli & Panci, 2009). This uses the second observational regions parameters of said paper.

With this, the same integral (4.10) can be calculated, resulting in the injection rates portrayed in Figure 5.7.

Similarly to the injection rates of the Solar System‘s bodies (Figure 5.5), the spectrum of positrons produced by the Milky Way starts in the energy range equal to $\gamma \sim 6 \cdot 10^2$, so beyond the low-energy positrons relevant for the production of 511 keV photons.

Summing all contributions over the entire spectrum (4.21) yields a total of $Q_{MW} = 8.39 \cdot 10^{-35} \, \frac{\mathrm{e}^+}{\mathrm{cm}^2\,\mathrm{s}}$, which is also about an order of magnitude greater than the total injection rate of the CPB. However the model of the Milky Way also includes the CMB component of the CPB radiation and the Galaxies value decreases with distance.

On the other hand, this model of the Milky Way only includes the infrared, optical and ultraviolet parts of the Galaxy‘s spectrum. Including the $\gamma$-ray spectrum of the Milky Way for example, would also further increase the yield of positrons. Considering that the Milky Way includes emissions in a wide range of frequencies similar to the CPB, but all magnitudes larger, than the same components of the CPB, the Milky Way interacting with itself, would yield greater positron yields than discussed in this thesis. This might

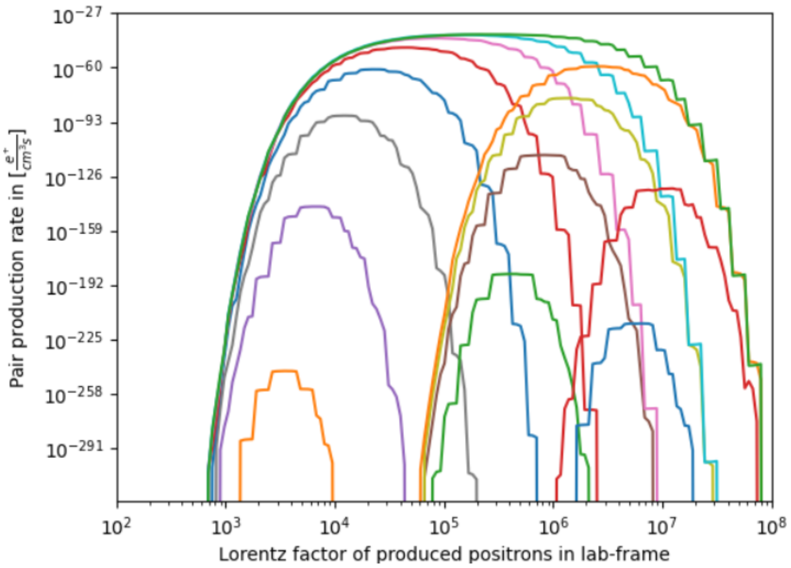

**Figure 5.7:** Injection rate of all blackbody combination between the CPB and the three blackbody Milky Way model. As with the solar system (Figure 5.5), the positrons only begin once they reach higher energies.

be research with interesting results, but which goes beyond the scope of this thesis.

# Chapter 6

# Diffusion and annihilation in the IGM

Now that a positron injection rate $Q(E,t) = \dot{n}(E)$ has been established, is stands to be seen, how this effects the positron‘s density throughout the IGM. For this, the steady state of the diffusion-loss equation (2.8) is assumed:

$$0 = \frac{d}{dE}[b(E)N(E)] + Q(E,t) \tag{6.1}$$

From here the positron density spectrum $n(E)$ in $[\frac{\mathrm{e}^+}{\mathrm{cm}^3}]$ is calculated by rearranging the above:

$$n(E) = -\frac{1}{b(E)} \int\limits_{E}^{E_{th}} Q(E)dE \tag{6.2}$$

$E_{th}$ describes the thermalization energy of the positrons, meaning the energy at which the positrons have cooled to the surrounding environment and are now viable for the annihilation process. For the array of temperatures, that are going to be looked at for the IGM, none lead to kinetic energies, that really compare to the resting energy of the positron. Even for the highest assumed temperature $T_{\mathrm{IGM}} = 10^7\,\mathrm{K}$, the ratio $\frac{E_{\mathrm{kin}}(T_{\mathrm{IGM}})}{E_0}$ is about $\sim 0.25\,\%$. Therefore the thermalization energy, or rather thermalization Lorentz factor will be chosen to be 1 for all temperatures. As the results calculated beforehand in this thesis all depend on $\gamma$ rather than E, the integral is substituted with $d\gamma = \frac{dE}{E_0}$ as follows:

$$n(\gamma) = -\frac{1}{b(E)} \int\limits_{\gamma}^{1} Q(E)E_0 d\gamma' \tag{6.3}$$

The resulting spectrum of positron densities can be seen below in Figure 6.1.

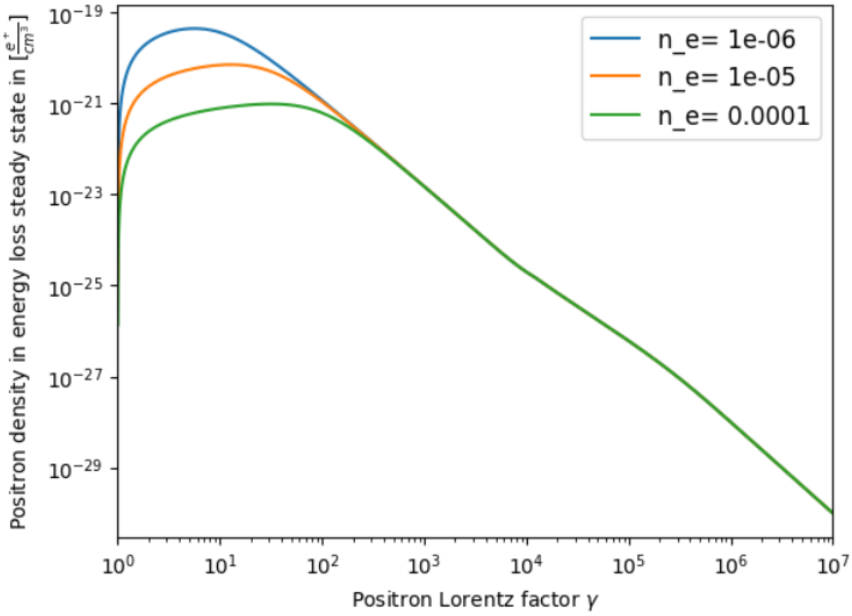

**Figure 6.1:** The three curves display the spectral positron density (6.3) for three different free electron densities within the IGM $n_e$. The magnetic field is set to be $B = 1\,\mu$G. Only low-energy positrons are affected by $n_e$ as this changes the impact of the Coulomb interactions, governing the low-energy particle's diffusion.

The maximum positron density settles in the energy range, where the main contribution to the energy loss is by Coulomb interactions, while the steeper falloff is mainly caused by Inverse Compton scattering. What is apparent from the figure is, that the free electron density $n_e$ only correlates to the positron density in the low-energy range. This stems from the direct proportionality between the energy loss through Coulomb interactions (2.9) and $n_e$.

Interesting for the annihilation process however is the diffusion-loss time scale $T_{\text{loss}}$, which describes the amount of time necessary for the produced positrons to lose enough energy, to thermalize in the surrounding IGM and become candidates for annihilation. The intuitive formula for $T_{\text{loss}}$ is:

$$T_{\text{loss}} = \int_{E}^{E_{\text{th}}} dt \tag{6.4}$$

With the energy loss $b(E)$ being defined as:

$$b(E) = -\frac{dE}{dt} \tag{6.5}$$

this can easily be substituted into the loss-time integral:

$$T_{\text{loss}} = \int_{E_{\text{th}}}^{E} \frac{dE'}{b(E')} = \int_{1}^{\gamma} \frac{E_0}{b(E')} d\gamma' \tag{6.6}$$

With (6.6) the diffusion-loss time scale for the entire energy spectrum of the injected positrons can be determined, as seen in Figure 6.2, for different densities of free electrons in the IGM $n_e$.

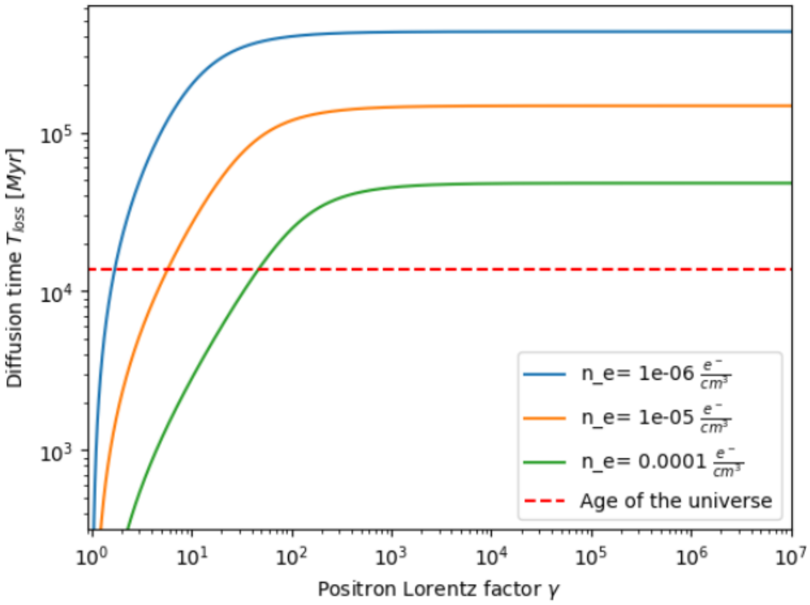

**Figure 6.2:** The diffusion time for different electron densities $n_e$ and different positron injection energies $\gamma$ is shown, with a magnetic field of $B = 1\,\mu G$ and an IGM particle density of $n_{IGM} = 10^{-5}\,\frac{1}{\mathrm{cm}^3}$. The horizontal line describes the age of the universe as reference. However positrons from so long ago are not considered in this thesis, as the CPB would have looked entirely different during their creation.

It is easy to see, that the times necessary for the positrons to thermalize are immense, so large in fact, that higher energy positrons produced with the beginning of the Universe would not have thermalized to this day. The assumed density of free electrons in the IGM has a significant impact on $T_{\mathrm{loss}}$. The other impactful parameter is the temperature of the $T_{\mathrm{IGM}}$, which becomes apparent when discussing the annihilation times.

After the time $T_{loss}$, the positrons have thermalized in the surrounding IGM with temperature $T_{\mathrm{IGM}}$. This is equivalent to $w = \frac{3}{2} k_B T_{\mathrm{IGM}}$ of thermal/kinetic energy for the positrons (Panther et al., 2018). After being thermalized, the properties of the IGM determine the annihilation time scale $\tau_{\mathrm{ann}}(w)$, meaning the average time needed for the positrons to annihilate with the surrounding medium (Panther et al., 2018):

$$\tau_{\mathrm{ann}}(w) = \left( c\beta(w) \sum_t \sigma_t(w) n_t \right)^{-1} \tag{6.7}$$

$t$ defines the target species, $\sigma_t(w)$ the species' cross section and $n_t$ its number density.

When approximating the IGM as only ionized hydrogen the only relevant species becomes the free electrons of the IGM. The only relevant cross sections in that case, are the cross sections for direct positron annihilation $\sigma_{\text{dir}}$ and radiative recombination $\sigma_{\text{ps}}$, forming positronium. Positronium is a bound state of an electron and a positron in a hydrogen like system. Due to annihilation, this atom is unstable (Schwarz et al., 2018). (6.7) can be reformed to:

$$\tau_{\text{ann}}(T) = \Big(n_e(\langle\sigma_{\text{dir}}v\rangle + \langle\sigma_{\text{ps}}v\rangle(T))\Big)^{-1} \tag{6.8}$$

where the cross sections have been rewritten as thermally averaged reaction rates using the temperature dependent particle speed $c\beta(w)$ and the Maxwell-Boltzmann distribution as the speed distribution. For $\langle\sigma_{\text{ps}}v\rangle$ the result from Gould (1989) is used:

$$\langle\sigma_{\text{ps}}v\rangle(T) = 4C\left(\frac{4k_BT}{\pi m}\right)^{1/2} \tilde{y}\,\phi(\tilde{y})\,\bar{g}(\tilde{y}) \tag{6.9}$$

with $\tilde{y} = \frac{Ry}{2k_BT}$. The averaged Gaunt factors $\bar{g}(\tilde{y})$ are set to be 0.9 regardless of the temperature, as they hardly affect the result. For temperatures up to $10^5\,\text{K}$, $\phi(\tilde{y})$ is approximated as follows (Gould, 1989):

$$\phi(\tilde{y}) = \frac{1}{2}(1.735 + \ln(\tilde{y} + (6\tilde{y})^{-1})) \tag{6.10}$$

while the function is changed to the power series for higher temperatures with the first seven summands in Gould (1989).

For direct annihilation, the cross section $\sigma_{\text{dir}} = \frac{\pi r_e^2}{\beta}$ is used as the non-relativistic approximation (Longair, 2011) and the thermally averaged reaction rate is calculated as in Guessoum et al. (2005):

$$\langle\sigma_{\text{dir}}v\rangle \approx 2\sqrt{\pi}\,0.34707\,r_{\text{e}}^2\,c \tag{6.11}$$

with the classical electron radius $r_{\text{e}}$. Finally summing the annihilation time with the diffusion time (Figure 6.2) for all combinations of IGM parameters yields Figure 6.3. Furthermore, the time the positrons need to cool down also gives an idea about the distance the particles are able to travel via diffusion in the IGM. For this, an equation describing diffusion in the IGM is:

$$D(E) = D_0\beta^{\eta} \tag{6.12}$$

$D_0$ is a diffusion constant in the IGM, for which $D_{0,1} = 10^{25}\,\frac{\text{cm}^2}{\text{s}}$ is chosen in the low-energy range (up to about $\gamma_c \sim 10^2$) and $D_{0,2} = 10^{29}\,\frac{\text{cm}^2}{\text{s}}$ beyond the lower energies. As there is not a lot of reference for IGM diffusion coefficients, both these values are guesses.

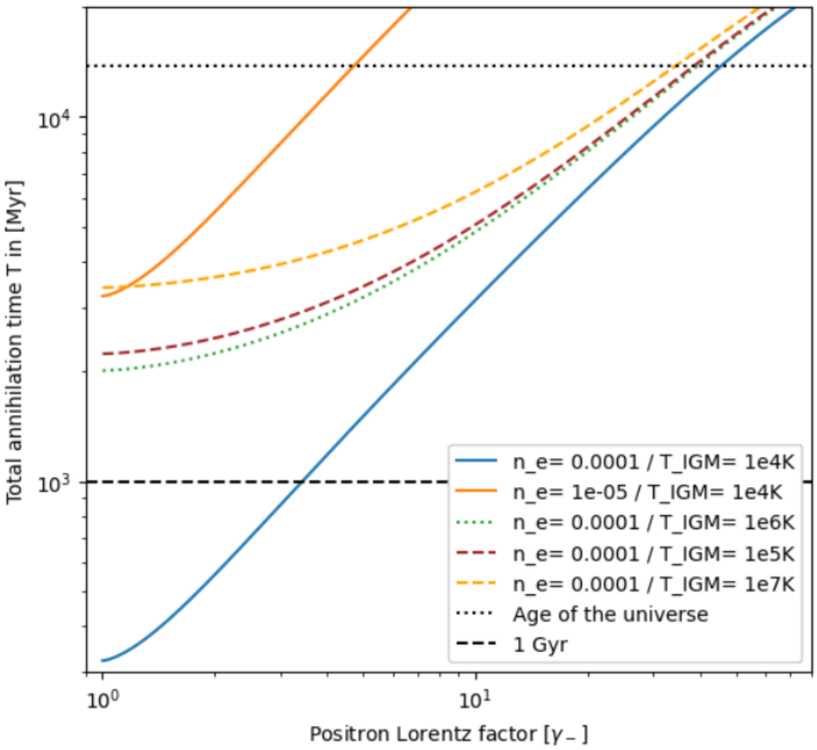

**Figure 6.3:** The graph shows the sum of diffusion times and annihilation times for all temperature and electron density combinations, that have times within the age of the Universe. The only positrons actually considered are ones up to an age of $\sim 1\,\mathrm{Gyr}$.

$\eta$ has the value $-\frac{3}{4}$ and $\beta$ is given by $\sqrt{1-\frac{1}{\gamma^2}}$. To avoid a sudden step in the function, the same is smoothed with the following expression:

$$D(E) = \frac{D_{0,1} + D_{0,2}(\gamma/\gamma_c)^k}{1 + (\gamma/\gamma_c)^k}\beta^\eta \tag{6.13}$$

where is $\gamma_c = 10^2$ as a rough separation between low- and high-energy particles and $k = 5$, which is choosen, soley based on its smoothing effect.
To arrive at the diffusion length scale $\lambda_\mathrm{D}^2$, following Fick's law $\lambda_D = \sqrt{6DT_\mathrm{loss}}$, the diffusion $D(E)$ has to be integrated over the energy spectrum, where the energy loss function $b(E)$ can be substituted in as:

$$\lambda_\mathrm{D}^2 = 6\int_0^{T_\mathrm{loss}} D(E)dt = 6\int_{E_\mathrm{th}}^{E} \frac{D(E')}{b(E')}dE' = 6\,E_0\int_1^{\gamma}\frac{D(E)}{b(E)}d\gamma' \tag{6.14}$$

For three spatial dimensions the formula is multiplied by 3. Just as for $T_\mathrm{loss}$, $\lambda_\mathrm{D}$ is plotted in Figure 6.4.
Figure 6.4 makes apparent, that despite the extraordinary diffusion times in Figure 6.2, the actual distance covered by the positrons via diffusion is comparably small. A possible

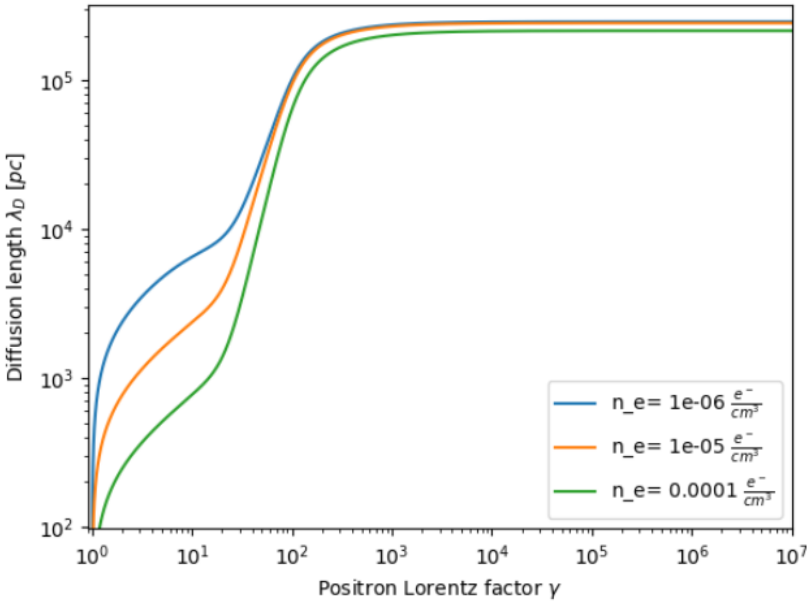

**Figure 6.4:** The diffusion length $\lambda_{\mathrm{D}}$ is portrayed here for the three different electron densities $n_e$. Note that the graph shows the square root of integral (6.14). The diffusion lengths are limited towards the higher end of the spectrum around $\sim 2.1 \cdot 10^5 - 2.5 \cdot 10^5$ pc.

explanation might be gyro movements of the particles due to the magnetic field in the IGM. To show the energy dependent relativistic gyro radii of the positrons the following is used:

$$r_g = \frac{\gamma m_e v_\perp}{eB} = \frac{m_e c\sqrt{\gamma^2 - 1}}{eB} \tag{6.15}$$

with the positrons mass $m_e$, the elementary charge $e$, the magnetic field $B = 10^{-10}\,\mathrm{T}$ and the velocity perpendicular to the magnetic field lines $v_\perp = c\beta$. The formula is simply derived by solving the equivalence equation of Lorentz force and centripetal force for the radius.

When only considering positrons, which have cooled and thermalized on a timescale, where cosmological redshift does not have to be accounted for yet, the oldest viable positrons have been created about 1 Gyr ago. Looking at Figure 6.3, only with an electron density $n_e = 10^{-4}\,\frac{\mathrm{e}^-}{\mathrm{cm}^3}$ and at an IGM temperature of $T_{\mathrm{IGM}} = 10^4\,\mathrm{K}$, can any created positron annihilate in this short timeframe. This includes positrons with energies up to a Lorentz factor of $\gamma = 3.43$. By integrating the positron density (Figure 6.1) up to this limiting $\gamma$ value and comparing to the entirety of the positron density, only $3.3 \cdot 10^{-4}$ of the positrons are viable for annihilation within this timeframe.

To finally calculate the total flux of positron annihilations, the following formula is used

$$F = \frac{1}{4\pi\,\mathrm{sr}} n_{e^-} n_{e^+} \langle \sigma_{\mathrm{tot}} v \rangle R \tag{6.16}$$

including the free electron density $n_{e^-} = 10^{-4}\,\frac{\mathrm{e}^-}{\mathrm{cm}^3}$, the positron density integrated up to

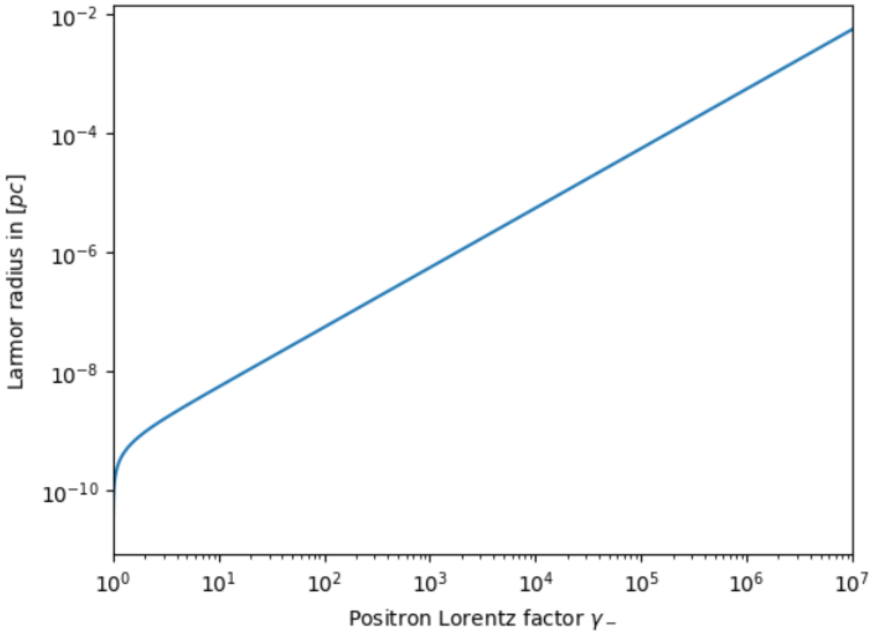

**Figure 6.5:** The curve shows the relativistic Larmor radii of the positrons moving through the magnetic field of the IGM.

the limiting $\gamma$ value $n_{e^+} = 6.30 \cdot 10^{-22}\,\frac{\mathrm{e}^+}{\mathrm{cm}^3}$, the total thermally averaged reaction rate at a mean temperature of $T = 10^4\,\mathrm{K}$: $\langle\sigma_{\mathrm{tot}}v\rangle$ and a distance $R$. Calculating the flux for a distance of $R = 10^3\,\mathrm{Mpc}$ yields a annihilation flux of $F = (1.5 \pm 0.2) \cdot 10^{-11}\,\frac{1}{\mathrm{s\,sr\,cm}^2}$. The uncertainty of the flux originates from Gaussian uncertainty propagation via:

$$\sigma_F = \frac{n_{e^-}}{4\pi\ sr}\langle\sigma_{tot}v\rangle R E_0 \cdot \left[\sum_p \sigma_p^2\left[\sum_k \frac{w_k}{b_k}\Big(\int_1^{\gamma_k}\frac{\partial Q}{\partial p}d\gamma_k\Big)\right]\right]^{1/2} \tag{6.17}$$

where $p$ numerates the parameters fitted to the injection rate $Q$ in Table 5.2 and their uncertainties $\sigma_p$, $b_k$ describes the value of $b(E)$ at $\gamma_k$ and $w_k$ is the width of the $\gamma$ steps. $\partial Q/\partial p$ are the partial derivatives of the function (5.1) by the different parameters $p$.

Of this total flux, the contribution of direct annihilations is only $F = (4.5 \pm 0.5) \cdot 10^{-14}\,\frac{1}{\mathrm{s\,sr\,cm}^2}$ or around 0.3 % of the total. This leaves most of the flux being the product of positronium formation and subsequent annihilation. The last mechanism to take into account at this point, is the differences between para-positronium (p-Ps) and ortho-positronium (o-Ps). The difference depends on the relative orientation of the particles spins, where parallel spins (S=1) result in o-Ps and antiparallel spins (S=0) result in p-Ps. This causes the decay rate of a base energy o-Ps to be $\lambda_o = 7.03996\,\mu s^{-1}$, while the same becomes $\lambda_p = 7989.62\,\mu s^{-1}$ for p-Ps. p-Ps decays into an even number of photons, mostly into two with 511 keV each in that case. o-Ps on the other hand decays into an odd number of photons, starting at three, with each photons energy therefore being $\leq 511\,\mathrm{keV}$ (Karshenboim, 2003). As 25 % of the formed positronium is of the p variety (Schwarz et al., 2018), only 25 % of the flux contributed by positronium formation and annihilation yields actual 511 keV photons. This leaves us with a theoretical flux of 511 keV photons created by the CPB radiation of $F_{511} = (7.6 \pm 0.8) \cdot 10^{-12}\,\frac{\mathrm{ph}}{\mathrm{s\,sr\,cm^2}}$. This is 25 % of the total annihilation flux, but multiplied by two, as any annihilation results in two separate photons. By multiplying the result with $4\pi$ to get $F_{511} = (1.0 \pm 0.1) \cdot 10^{-10}\,\frac{\mathrm{ph}}{\mathrm{s\,cm^2}}$, the flux can be compared to fluxes measured in the Milky Way. For example, the two-shell bulge-only model calculated in Weidenspointner et al. (2007), displaying the brightness of the galactic bulge region in annihilation radiation, has a flux of $(0.96 \pm 0.06) \cdot 10^{-3}\,\frac{\mathrm{ph}}{\mathrm{s\,cm^2}}$. Compared to the bright bulge region of the Milky Way, the background annihilation radiation is magnitudes below and is therefore probably less influential on measurements of that region. Even looking at all the other calculated shell models presented in Weidenspointner et al. (2007), fluxes are at their smallest still of the magnitude $\sim 10^{-4}\,\frac{\mathrm{ph}}{\mathrm{s\,cm^2}}$ and thereby above the calculated 511 keV flux of the background radiation.

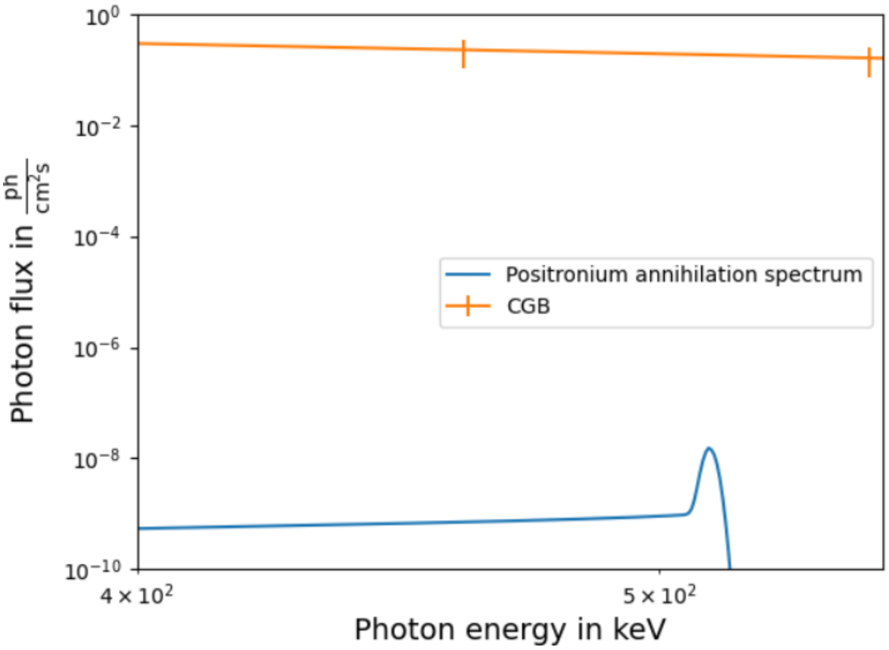

**Figure 6.6:** The above compares the photon fluxes of the CPB‘s $\gamma$-ray component (orange) and the positronium spectrum (blue). The calculated positronium spectrum is clearly outshone, with the CGB‘s flux being $\sim 10^7$ greater than even the 511 keV. The 511 keV line itself is plotted as a Gaussian line with a width of 1.4 keV.

Looking at Figure 6.6, it becomes apparent, that in the realm of the approximations made in this thesis, the produced positron annihilation spectrum is outshone by the CGB component by a magnitude of about $10^7$ at the 511 keV line, meaning the background annihilation flux is far below what happens around AGNs, especially Seyfert Galaxies in this energy range (see Figure 2.2).

# Chapter 7

# Conclusion and future prospects

To summarize: Calculating the spectral positron injection rate from the CPBs photons colliding with each other, results in a spectrum (Figure 5.1) starting at low-energy positrons, that are basically at rest, going up to about energies equal to about $\gamma \approx 10^6$. However most positrons injected are of the low-energy variety. Furthermore, summing over the total energy spectrum gives a total injection rate of $Q = (2.0 \pm 0.5) \cdot 10^{-36}\,\frac{\mathrm{e}^+}{\mathrm{cm}^3\mathrm{s}}$.
In comparison, the injection rates of positrons, created by the Solar System‘s (mainly the Sun) and the Milky Way‘s photons interacting with the CPBs photons, yields higher totals than the CPB alone, but the produced positrons only start at energies around $\gamma \approx 3 \cdot 10^3$ or $\gamma \approx 6 \cdot 10^2$ respectively, when only taking the IR, optical and UV components into consideration. It is therefore reasonable to assume, that both these sources only outshine the CPBs low-energy positrons, when taking all their components (e.g. $\gamma$-rays) into consideration.
Further investigating the way the produced positrons diffuse and annihilate within the IGM, carries further consequences for the particles. For one, the diffusion time $T_{\mathrm{loss}}$ of positrons in the IGM heavily depends on the free electron density $n_e$, although the produced timescales are very large regardless of the $n_e$. According to the results any positrons beyond lower energy ranges would take longer to thermalize within the IGM, than the age of the observable Universe. On top of the time necessary for thermalization, the timescale for the positrons to annihilate with free electrons $\tau_{\mathrm{ann}}$ has also been analysed. Adding both times until the positrons annihilate into the sought after photons, has the consequence, that when only considering positrons with a maximum age of 1 Gyr, only 0.033 % of the total produced positron density is viable. Despite the immense timescales needed for the positrons to thermalize in the IGM, the actual distance they traverse is surprisingly small, with the particles being subject to gyro movements induced by the IGMs magnetic field.
The remaining flux of annihilations is $F = (1.5 \pm 0.2) \cdot 10^{-11}\,\frac{1}{\mathrm{s\,sr\,cm}^2}$, of which only $F_{511} = (7.6 \pm 0.8) \cdot 10^{-12}\,\frac{1}{\mathrm{s\,sr\,cm}^2}$ are actually 511 keV photons. Compared to measure-

ments of the galactic annihilation radiation flux of 511 keV photons, the background flux of photons is $\sim 10^4$ orders of magnitude below even the dimmer regions of the Milky Way.

If one were to improve upon the here presented results in the future, there are some obvious parts to be tackled. It hardly needs to be pointed out, that should measurements of the CPB, especially the COB and CUB components, become more precise in the future, this would trickle down into a more precise result, however a result of the same order of magnitude. Furthermore, one may expand upon the analysis and discussion of the diffusion of positrons within the IGM. More mechanisms of energy loss could be considered and also more realistic approximations of the composition of the IGM could be considered, possibly reducing thermalization times and therefore increasing the annihilation flux. For example including non-ionized atoms carrying bound electrons or even simulating the plasma of the IGM with these components.

Seeing as the CPB radiation is present everywhere and not only in the vicinity of the IGM, one may also consider what would happen to positrons created in the ISM for example.

Also including more components of the Milky Way photon field would increase the local positron production within the Milky Way, although probably without much impact on the isotropic CPB background.

As has been discussed in section 4, the photon densities of emitters (here CPB) are easily interchangeable within the yield integral. Therefore one could reproduce the work and analysis above with, for example, the Milky Way interacting with itself to create positrons. This would lead to different injection spectra within a different medium, producing new annihilation fluxes.

A last idea to consider might be, to work on the restriction set within this thesis. In all the above, everything happens on scales, where cosmological redshift can be neglected. Therefore thermalized positrons cannot be infinitely old, reducing the amount of viable positrons. By introducing cosmology into the CPB model, one might adapt the given model for different values of redshift, changing its shape and values. Furthermore the surrounding medium in which such positrons would be injected to, would be different, once again changing the way these particle thermalize.

# Chapter 8

# Summary

## 8.1 English summary

After a brief introduction, a summary of the Cosmic Photon Background (CPB) is given. This includes the various components it is composed off, as well as their respective sources and the way they are either measured or estimated. This is followed by an introduction into the Dirac equation, leading to the idea of matter-antimatter creation through photon collision, as well as the inverse process of annihilation, mainly the Breit-Wheeler process. The theory part is concluded with a derivation of the diffusion-loss equation and further with a brief rundown of the different mechanisms, by which positrons flying through the intergalactic medium (IGM) lose energy, given a certain set of parameters.

The following chapter describes the blackbody radiator, its relevance in describing the Cosmic Microwave Background (CMB) and how it can be used to model the entirety of the CPB spectrum. This is followed by the methods, with which the sum of blackbodies is fitted to the CPB spectrum and how this can be used to already estimate a total injection rate of positrons.

This is then followed up by an explanation of the cross section of the photon-photon pair production, leading into a brief derivation of the ultimately used yield integral. With the formula of the integral in place, the next section details how the integral is actually calculated as well as how the resulting errors and error propagation are treated.

With all the explanation in place, the following chapter presents the results of various calculations using the yield integral. This includes the produced spectral positron injection rate created by the CPB interacting with itself, which is additionally fitted with a function to make following calculations more accessible. The entire injection rate is summed up to then be compared to the positron injection rate of the solar systems bodies. For this, all their positron fluxes and luminosities are calculated along a line of sight, which are then compared to the same of the CPB. Lastly the positron injection rate of the Milky Way

Galaxys radiation interacting with the CPB is analysed.
Beyond that, the diffusion time for the positrons to thermalize in the IGM is calculated, as well as the distance they travel within that time period. Additionally the annihilation time for thermalized positrons with free electrons is determined. On the basis of these results, only a small fraction of CPB-produced positrons remains viable for annihilation, of which even less actually yield 511 keV photons (due to different forms of positronium decay), the flux of which is finally determined.
The thesis is rounded out by a short recapitulation of the results and their implications for the analysis of the 511 keV line within our galaxy. Furthermore, future expansion ideas as well as improvements to the presented work are given.

## 8.2 Deutsche Zusammenfassung

Nach einer kurzen Einführung, wird der Kosmische Photonen Hintergrund (CPB) zusammengefasst. Dies umfasst die verschiedenen spektralen Komponenten des CPB, sowie die Methoden mit welchen selbige gemessen oder deren Ober-/Untergrenzen bestimmt werden. Hierauf folgt eine Einführung zur Dirac Gleichung mitsamt der Idee der Kreation von Materie-Antimaterie Paaren durch Photonenkollisionen und dessen inversen Prozesses der Pärchen-Annihilation, vor Allem in Form von dem Breit-Wheeler Prozess. Die Theoriesektion wird abgeschlossen mit einer Herleitung der Konvektions-Diffusions-Gleichung und einer Erläuterung der verschiedenen Energieverlust Mechanismen von Positronen in dem Intergalaktischen Medium (IGM) auf Basis eines Satzes an Parametern.
Der folgende Abschnitt erläutert den Schwarzkörper Strahler, sowie dessen Relevanz in Hinsicht auf das Beschreiben der Kosmischen Mikrowellen Hintergrundstrahlung (CMB). Des Weiteren wird beschrieben wie der gute Fit des Schwarzkörpers auf den CMB auf den restlichen CPB erweitert werden kann, um diesen vollständig zu beschreiben. Daraufhin werden die Methoden mit welchen das Schwarzkörpermodell an den CPB angepasst wird erklärt. Mit den Ergebnissen wird eine erste Abschätzung der Positronen Injektionsrate durch den CPB aufgestellt.
Weiter wird der Wirkungsquerschnitt für die Photonen-Photonen Paar Produktion geschildert. Darauf aufbauend wird das Positronen-Kreations Integral aufgestellt und dessen Berechnung erläutert, sowie wie mit den resultierenden Fehlern und Fehlerfortpflanzungen umgegangen wird.
Mit der Vorarbeit erledigt, werden im folgenden Kapitel die Ergebnisse des Integrals präsentiert. Primär umfasst dies die spektrale Injektionsrate von Positronen, die von dem CPB kreiert werden. Zusätzlich wird an dieses Ergebnis eine Kurve angepasst, um später folgende Rechnungen zugänglicher zu machen. Um die Injektionsrate des CPB mit der selben des Sonnesystems zu vergleichen, werden die Werte entlang des Energiespektrums

aufsummiert. Die Ergebnisse der Körper des Sonnensystems werden zu Flüssen und Helligkeiten per Sichlinienintegration weiterverwendet, um sie daraufhin mit denen des CPBs zu vergleichen. Zuletzt wird auch die Injektionsrate der Milchstraße untersucht.

Auf der Injektionsrate aufbauend, wird die Diffusionszeit bis zur Thermalisierung der Positronen im IGM bestimmt, sowie die Distanz die selbige in dieser Zeitspanne zurücklegen. Zusätzlich wird die Annihilationzeit der thermalisierten Positronen mit freien Elektronen berechnet. Hierduch bleibt nur ein kleiner Anteil der produzierten Positronen zur Annihilation relevant. Hiervon trägt wiederum auch nur ein Anteil zur tatsächlichen Kreation von 511 keV Photonen bei, aufgrund der verschieden Zerfallsprozesse von Positronium. Zuletzt wird der finale Fluss an 511 keV Photonen berechnet.

Die Arbeit wird abgerundet durch eine kurze Rekapitulation der Ergebnisse und deren Implikationen für die Suche der Quellen der galaktischen 511 keV Linie. Am Ende werden mögliche Verbesserungen, Erweiterungen und alternative Routen der Arbeit vorgeschlagen.

# Declaration of originality

I declare that I have authored this thesis independently, that I have not used any other than the declared sources / resources, and that I have explicitly marked all material which has been quoted either literally or by content from the used sources. I also declare that this thesis has not been submitted to any other examination authorities.

Würzburg, January 21, 2025

Name ........SPenny........................

# Bibliography

Andika Irham T. (2016). On the Nature of Type 1 AGN: Emission Properties and Correlations. DOI:10.13140/RG.2.2.23303.80809. `https://www.researchgate.net/publication/306344484_On_the_Nature_of_Type_1_AGN_Emission_Properties_and_Correlations`

Atkins P. W. (1991). Quanta: A Handbook of Concepts.Oxford [England]; New York : Oxford University Press. ISBN 9780198555728. `https://archive.org/details/quantahandbookof00atki/mode`

Atkinson Kendall E. (1989). An Introduction to Numerical Analysis (2nd ed.) John Wiley & Sons, New York. ISBN 0471500232.

Böttcher M., Schlickeiser R. (1997). The Pair Production Spectrum from Photon-Photon annihilation. arXiv:astro-ph/9703069v1. `https://doi.org/10.48550/arXiv.astro-ph/9703069`

Breit G., Wheeler John A. (1934). Collision of Two Light Quanta. Physical Review, vol. 46, Issue 12, pp. 1087-1091. `https://ui.adsabs.harvard.edu/abs/1934PhRv...46.1087B`

Marco Cirelli, Paolo Panci (2001). Inverse Compton constraints on the Dark Matter $e^{\pm}$ excesses. arXiv:0904.3830v3. `https://doi.org/10.48550/arXiv.0904.3830`

Dicke R. H., Peebles P. J. E., Roll P. G., Wilkinson D. T. (1965). Cosmic Black-Body Radiation. Astrophysical Journal, vol. 142, p.414-419. `https://ui.adsabs.harvard.edu/abs/1965ApJ...142..414D`

Dirac P.A.M. (1930). On the Annihilation of Electrons and Protons. Mathematical Proceedings of the Cambridge Philosophical Society, Volume 26, Issue 3, July 1930, pp. 361 - 375. `https://doi.org/10.1017/S0305004100016091`

Dirac P.A.M. (1931). Quantised singularities in the electromagnetic field. 01 September 1931, Volume 133, Issue 821. `https://doi.org/10.1098/rspa.1931.0130`

Esnault L., d‘Humieres E., Arefiev A., Riberyre X. (2021). Electron-positron pair production in the collision of real photon beams with wide energy distributions. arXiv:2103.09099v1. `https://arxiv.org/pdf/2103.09099`

Gould Robert J. (1989). Direct Positron Annihilation and Positronium Formation in Thermal Plasmas. Astrophysical Journal, 344, 232-238. `http://dx.doi.org/10.1086/167792`

He Y., Blackburn T. G.,Toncian T., Arefiev A. (2022). Achieving pair creation via linear and nonlinear Breit–Wheeler processes in dense plasmas irradiated by high-intensity laser pulses. Phys. Plasmas 1 May 2022; 29 (5): 053105. `https://doi.org/10.1063/5.0086577`

N. Guessoum, P. Jean, W. Gillard (2005). The lives and deaths of positrons in the interstellar medium. arXiv:astro-ph/0504186v1. `https://doi.org/10.48550/arXiv.astro-ph/0504186`

Ryley Hill, Kiyoshi W. Masui and Douglas Scott (2018). The Spectrum of the Universe. arXiv:1802.03694v2. `https://doi.org/10.48550/arXiv.1802.03694`

Inoue Yoshiyuki (2014). Cosmic Gamma-ray Background Radiation. arXiv:1412.3886v1. `https://doi.org/10.48550/arXiv.1412.3886`

Johnson W. N. III. Harnden F. R. Jr.. Haymes R. C. (1972). The Spectrum of Low-Energy Gamma Radiation from the Galactic-Center Region. Astrophysical Journal, vol. 172, p.L1. `https://ui.adsabs.harvard.edu/abs/1972ApJ...172L...1J`

Karshenboim S. G. (2003). Precision Study of Positronium: Testing Bound State QED Theory. arXiv:hep-ph/0310099v1. `https://doi.org/10.48550/arXiv.hep-ph/0310099`

Krumholz Mark R., Crocker Roland M., Sampson Matt L. (2022). Cosmic Ray Interstellar Propagation Tool using Itô Calculus (criptic): software for simultaneous calculation of cosmic ray transport and observational signatures. arXiv:2207.13838v2. `https://doi.org/10.48550/arXiv.2207.13838`

Guilaine Lagache, Jean-Loup Puget, and Hervé Dole (2005). Dusty Infrared Galaxies: Sources of the Cosmic Infrared Background. Annual Review of Astronomy and Astrophysics, Vol. 43:727-768. `https://doi.org/10.1146/annurev.astro.43.072103.150606`

Leventhal M., MacCallum C. J., Stang P. D. (1978). Detection of 511 keV positron annihilation radiation from the galactic center direction. Astrophysical Journal, Vol. 225, p. L11-L14 (1978). `https://ui.adsabs.harvard.edu/abs/1978ApJ...225L..11L`

Longair Malcom S. (2011). High Energy Astrophysics 3rd edn. Cambridge University Press. Online ISBN 9780511778346. `https://doi.org/10.1017/CBO9780511778346`

Panther Fiona H., Seitenzahl Ivo R., Crocker Roland M., Machacek Joshua R., Murtagh Dan J., Siegert Thomas, Diehl Roland (2018). The effect of positron-alkali metal atom interactions in the diffuse ISM. arXiv:1807.01880v1. `https://doi.org/10.1103/PhysRevD.98.023015`

Penzias A. A., Wilson R. W. (1965). A Measurement of Excess Antenna Temperature at 4080 Mc/s. Astrophysical Journal, vol. 142, p.419-421. `https://ui.adsabs.harvard.edu/abs/1965ApJ...142..419P`

Petrov G. T., ed. (2004). Active Galaxy Nuclei. Bulgarian Academy of Sciences/Institute of Astronomy. `http://www.astro.bas.bg/~petrov/galaxies_files/agn.html`

Prantzos N., Boehm C., Bykov A. M., Diehl R., Ferriere K., Guessoum N., Jean P., Knoedlseder J., Marcowith A., Moskalenko I. V., Strong A., Weidenspointner G. (2010). The 511 keV emission from positron annihilation in the Galaxy. arXiv:1009.4620. `https://doi.org/10.48550/arXiv.1009.4620`

Ribeyre X., d'Humières E., Jansen O., Jequier S., Tikhonchuk V. T., Lobet M. (2016). Pair creation in collision of $\gamma$-ray beams produced with high-intensity lasers. `https://doi.org/10.1103/physreve.93.013201`

Schwarz Mario, Franke Sabrina M., Oberauer Lothar, Plein Miriam D., Steiger Hans Th. J., Tippmann Marc (2018). Measurements of the Lifetime of Orthopositronium in the LAB-based Liquid Scintillator of JUNO. arXiv:1804.09456v1. `https://doi.org/10.48550/arXiv.1804.09456`

Siegert Thomas (2023). The Positron Puzzle. arXiv:2303.15582v1. `https://doi.org/10.48550/arXiv.2303.15582`

Siegert Thomas (2024). Time-variable diffuse $\gamma$-ray foreground. Monthly Notices of the Royal Astronomical Society, Volume 533, Issue 1, September 2024, Pages 165–183. `https://doi.org/10.1093/mnras/stae1742`

Titov A. I., Kampfer B., Takabe H., Hosaka A. (2013). Breit-Wheeler process in very short electromagnetic pulses. arXiv:1303.6487v1. `https://doi.org/10.48550/arXiv.1303.6487`

Weidenspointner G., Knödelseder J., Jean P., Skinner G. K., Roques J.-P., Vedrenne G., Milne P., Teegarden B. J., Diehl R., Strong A., Schanne S., Cordier B., Winkler C. (2007). The sky distribution of 511 keV positron annihilation line emission as measured with INTEGRAL/SPI. arXiv:astro-ph/0702621v1. `https://doi.org/10.48550/arXiv.astro-ph/0702621`

Weidenspointner G., Skinner G. K., Jean P., Knödelseder J., von Ballmoos P., Diehl R., Strong A., Cordier A., Cordier B., Schanne S., Winkler C. (2008). Positron astronomy with SPI/INTEGRAL. New Astronomy Reviews, Volume 52, Issues 7–10, October 2008, Pages 454-456. `https://doi.org/10.1016/j.newar.2008.06.019`